Shear rheology of a dilute suspension of thin rings

Neeraj S. Borker and Donald L. Koch

Citation: Journal of Rheology **67**, 723 (2023); doi: 10.1122/8.0000628
View online: https://doi.org/10.1122/8.0000628
View Table of Contents: https://sor.scitation.org/toc/jor/67/3
Published by the The Society of Rheology

Shear rheology of a dilute suspension of thin rings

Neeraj S. Borker[1] and Donald L. Koch[2,a)]

[1]*Sibley School of Mechanical and Aerospace Engineering, Cornell University, Ithaca, New York 14853*
[2]*Robert Frederick Smith School of Chemical and Biomolecular Engineering, Cornell University, Ithaca, New York 14853*

(Received 6 January 2023; published 14 April 2023)

Abstract

The rheology of suspensions of rings (tori) rotating in an unbounded low Reynolds number simple shear flow is calculated using numerical simulations at dilute particle number densities ($n \ll 1$). Suspensions of non-Brownian rings are studied by computing pair interactions that include hydrodynamic interactions modeled using slender body theory and particle collisions modeled using a short-range repulsive force. Particle contact and hydrodynamic interactions were found to have comparable influences on the steady-state Jeffery orbit distribution. The average tilt of the ring away from the flow-vorticity plane increased during pairwise interactions compared to the tilt associated with Jeffery rotation and the steady-state orbit distribution. Particle stresses associated with the increased tilt during the interaction were found to be comparable to the stresses induced directly by particle contact forces and the hydrodynamic velocity disturbances of other particles. The hydrodynamic diffusivity coefficients in the gradient and vorticity directions were also obtained and were found to be two orders of magnitude larger than the corresponding values in fiber suspensions at the same particle concentrations. Rotary Brownian dynamics simulations of isolated Brownian rings were used to understand the shear rate dependence of suspension rheology. The orbit distribution observed in the regime of weak Brownian motion, $Pe \gg \phi_T^{-3}$, was surprisingly similar to that obtained from pairwise interaction calculations of non-Brownian rings. Here, the Peclet number Pe is the ratio of the shear rate and the rotary diffusivity of the particle and ϕ_T is the effective inverse-aspect ratio of the particle (approximately equal to 2π times the inverse of its non-dimensional Jeffery time period). Thus, the rheology results obtained from pairwise interactions should retain accuracy even for weakly Brownian rings ($n \ll 1$ and $\phi_T^{-3} \ll Pe$).
https://doi.org/10.1122/8.0000628

I. INTRODUCTION

Suspensions of high-aspect ratio particles are useful in a number of practical applications such as fabrication of high-strength composites [1], production of conducting optical films used in touchscreen devices [2], or paper making [3]. A simple shear flow is a linear approximation to a pressure-driven flow found in injection molding or casting systems. A detailed understanding of the orientational dynamics of individual particles in a shear flow can be used to obtain the microstructure and material properties of the final processed product. In this paper, the shear-induced orientation and rheology of a dilute suspension of high-aspect ratio rings with circular cross section is calculated through dynamic numerical simulations of pairwise interactions that include both *long-range hydrodynamic interactions* modeled in the slender body theory framework and *particle contacts* modeled using a short-range repulsive force. The numerical simulations suggest that particle contact between rings is relevant in describing the orientational structure of the particles even at dilute particle concentrations ($n \ll 1$), where n is the non-dimensional number density normalized by the inverse cube of the largest dimension of the particle. This starkly differs from dilute fiber suspensions wherein particle contacts are rare in the dilute limit and steady-state orientation distribution can be described by considering purely hydrodynamic interactions. The steady-state orientation distribution was obtained through a large number of dynamic pairwise interaction simulations, and this orbit distribution was used to compute the $O(n)$ correction to the shear viscosity of the suspension. Another set of dynamic simulations, initialized with the steady-state orbit distribution, was then used to compute the $O(n^2)$ correction to the viscosity and the normal stresses that result from transient changes in the stresses on the particle surface during interactions. Rotary Brownian dynamics simulations of isolated Brownian rings were also performed to obtain the shear rate dependence of the orientation distribution along with shear and normal stresses induced by the particles. The shear rheology of weakly Brownian particles in the shear-dominated regime was also compared to the results set by the orbit distribution due to pairwise interactions of non-Brownian rings.

The rheology of rigid particles remains an area of active research. The $O(n)$ correction to viscosity of a dilute suspension of spheres was obtained by Einstein [4]. Over the century following Einstein's seminal paper, extensive theoretical, simulation, and experimental work has been carried out on this subject at all particle concentrations for both Brownian and non-Brownian spheres that are summarized in many review articles [5,6]. The rheology of a suspension of thin fibers was also extensively studied leading to a detailed understanding of the variation in the microstructure,

a)Author to whom correspondence should be addressed; electronic mail: dlk15@cornell.edu

viscosity, and normal stress differences with the aspect ratio and particle concentration summarized in review papers of Refs. [7] and [8]. The rheology of moderate aspect ratio disks has been studied, although less extensively, through experimental and simulation works [9–16].

In fiber suspensions at dilute ($n \ll 1$) and semidilute ($n = O(1)$, $n \ll O(\bar{A})$) concentrations purely hydrodynamic interactions between particles determine the suspension rheology. Here, $\bar{A} > 1$ is the fiber aspect ratio. In the semiconcentrated ($n = O(\bar{A})$) or concentrated ($n = O(\bar{A}^2)$)) regime, mechanical contacts between particles also have a strong influence. In contrast, even in the dilute regime, the mechanical collision rate between disks [17] has the same scaling as the frequency of the most important hydrodynamic interactions, i.e., interactions between a tumbling and an aligned disk [justified in Sec. II A]. Thus, mechanical contacts in planar particles such as disks (or rings) greatly influence the steady-state orientation distribution. Additionally, tumbling disks generate large $O(1)$ velocity disturbances (normalized by the product of the shear rate and largest particle dimensions) compared to the weaker $O(\ln(\bar{A})^{-1})$ velocity disturbance generated by fibers. The $O(n)$ viscosity correction of fiber suspensions based on the orbit distribution set by weak hydrodynamic interactions is $O(\ln(\bar{A})^{-1}\bar{A}^{-1})$. A similar calculation is unavailable for disk suspensions, but the particle stress is expected to have a larger magnitude than the fiber result at the same concentration [18]. The rheology of suspension of particles with these two shapes is driven by different physical mechanisms and thereby have startling differences.

The rheological understanding of suspensions of fibers and disks does not directly translate into an understanding of the rheology of rings, although rings have geometric similarities to both disks and fibers. Rings generate weak velocity disturbances similar to fibers but rotate like disks in a simple-shear-flow. Particle contact should play a critical role in orientation distribution and suspension stresses for rings as they do for disks. The current work fills this gap of understanding and elucidates similarities and differences between ring suspensions and suspensions of fibers and disks.

High-aspect ratio ring suspensions have the unique property that they retain low volume fractions of $O(\bar{A}^{-1})$ even at close packing because of the large hole and nature of the excluded volume interactions [19]. For example, ring suspensions could be used to make highly porous materials for CO_2 capture applications [20] through solvent evaporation [21] or phase-separation [22] methods on a processing line. Another application involves making composite materials with bidirectionally uniform mechanical strength [1] or conducting films with bidirectionally isotropic conductivity in electronics [2], both of which could be made with injection molding or casting processes.

Purely hydrodynamic interactions modeled through slender body theory (SBT) have been successfully applied to predict the rheology of fiber suspensions at dilute ($n \ll 1$) and semidilute concentrations ($n \ll \bar{A}$) [23]. The SBT formulation of Mackaplow and Shaqfeh (1996) [23] combined with the orientation distribution calculations of [24] in dilute and semidilute regimes accurately predicts the viscosity correction for fibers obtained experimentally [25]. The viscosity of a semidilute suspension of non-contacting spheroids obtained using SBT also aligns well with the values obtained from Monte Carlo Stokesian dynamics simulations [26,23]. On the other hand, calculations based on pure hydrodynamic particle interactions underpredict the rheological properties compared with experimental data in the semiconcentrated regime ($n = O(\bar{A})$) wherein a multiparticle contact is expected to hinder free rotation of particles. Inclusion of stresses from mechanical contacts shows good agreement with experimental data [27–29]. Recent numerical simulations of [29] also demonstrated that the leading order velocity disturbance from SBT and excluded volume interactions are sufficient to compute the rheology of contacting fibers in the semiconcentrated regime.

For non-straight slender bodies such as rings, unlike straight fibers, particle contact is equally important to hydrodynamic interactions even in the dilute regime ($n \ll 1$). The velocity disturbance generated by the local section of a high-aspect ratio slender ring is of the same order of magnitude as that generated by a straight fiber, and thus, the hydrodynamic interaction between rings should be accurately captured by SBT. Particle contact is captured by using a short-range repulsive force similar to the one used in numerical simulations for studying disks approximated by a planar collection of spheres [10].

Sections II and III of this paper introduce the simulation methodology and present the results of simulations, respectively. Jeffery's solution for rotation of isolated axisymmetric particles is briefly discussed in Sec. II A. Section II B describes the numerical scheme for simulating pairwise interaction between rings and obtaining particle properties from corresponding particle trajectories. The procedure for calculating the average stress in the suspension that involves a renormalization process for obtaining an absolutely convergent integral is described in Sec. II C. A procedure for computing steady state orientation distribution from pairwise interaction calculations is established in Sec. II D. The qualitative characteristics of contacting and non-contacting particle trajectories are described using simulation results in Sec. III A. The values of the collision frequency and hydrodynamic diffusivity are discussed in Sec. III B. The orientational microstructure of the particles that includes transient effects of pairwise interactions is described in Sec. III C. This is followed by a discussion of the suspension viscosity and normal stress differences in ring suspensions correct to $O(n^2)$ in Secs. III D and III E, respectively. The shear rate dependence of suspension rheology of Brownian rings is briefly discussed in Sec. III F. Section III F also discusses the similarity of orientation distribution between the non-Brownian rings and the classic result of Leal and Hinch for weakly Brownian rings [30], expanding the range of applicability of our pairwise simulation results. The rheology of ring suspension is also compared with the values of corresponding properties for equivalent fiber and disk suspensions wherever applicable. In Sec. IV, conclusions of the study are outlined followed by possible directions for future research.

Throughout this study, time is non-dimensionalized by the inverse of the shear rate γ^{-1}, lengths are non-dimensionalized by half the extent of the particle in the plane of the ring, $\bar{R} = (R + a)$, and stresses are non-dimensionalized by $\mu_f\gamma$, where μ_f is the fluid viscosity, R is the radius of curvature of the centerline of the ring cross section, and a is the radius of

the ring cross section. The non-dimensional number density is $n = n^* \bar{R}^3$, with n^* being the dimensional number density. The particle aspect ratio $\bar{A} = (R + a)/a$ is defined as the ratio of the extent of the particle in the plane of the ring and its extent perpendicular to the plane. A *slender body aspect ratio* $A = R/a$ is also used as it naturally occurs in slender body equations for a torus [31] and is related to the particle aspect ratio through the relation: $\bar{A} = A + 1$. We will also consider an effective *inverse*-aspect ratio, $\phi_T (< 1)$, which is defined as the ratio of the smallest to largest dimension of an oblate spheroid that rotates with the same Jeffery period as the torus. The aspect ratio of an equivalent fiber or disk is simply the particle extent in the long direction divided by the particle extent in the short direction and is equivalent to $\bar{A}$. The fiber half-length and the disk radius are used to non-dimensionalize the length scale of these particles, respectively. Three coordinate systems, as shown in Fig. 1(a), are used in this study wherever applicable: a global coordinate system defined by the flow (1 or $\hat{\boldsymbol{U}}_\infty$), vorticity (2 or $\hat{\boldsymbol{\Omega}}_\infty$), and gradient direction (3 or $\hat{\boldsymbol{\Gamma}}_\infty$) of the simple shear flow; a particle coordinate system defined by the orientation of the axis of symmetry $\boldsymbol{p}$, the projection of the flow direction of the simple shear flow in the plane of the ring $\boldsymbol{n} = (\boldsymbol{I} - \boldsymbol{pp}) \cdot \hat{\boldsymbol{U}}_\infty / |(\boldsymbol{I} - \boldsymbol{pp}) \cdot \hat{\boldsymbol{U}}_\infty|$, and $\boldsymbol{b} = \boldsymbol{p} \times \boldsymbol{n}$; and a local-SBT-coordinate system defined by $\boldsymbol{p}$, the tangent to the ring centerline $\boldsymbol{e}_z$, and a vector $\boldsymbol{p} \times \boldsymbol{e}_z$.

II. SIMULATION METHOD FOR PAIRWISE INTERACTIONS

A. Jeffery orbits of isolated rings in a simple shear flow

The rate of change of the orientation of the axis of symmetry $\boldsymbol{p}$ of any axisymmetric particle in a simple shear flow (SSF), $\boldsymbol{u}_\infty = \boldsymbol{r} \cdot \hat{\boldsymbol{\Gamma}}_\infty \hat{\boldsymbol{U}}_\infty$ [32,33], is termed as *Jeffery rotation* $\dot{\boldsymbol{p}}_J$ and is given by

$$\dot{\boldsymbol{p}}_J(\boldsymbol{p}) = \boldsymbol{p} \cdot \boldsymbol{R}_\infty + \lambda(\boldsymbol{E}_\infty \cdot \boldsymbol{p} - \boldsymbol{E}_\infty : \boldsymbol{ppp}), \tag{2.1}$$

where $\boldsymbol{R}_\infty = 0.5(\nabla \boldsymbol{u}_\infty - (\nabla \boldsymbol{u}_\infty)^T)$ is the vorticity tensor; $\boldsymbol{E}_\infty = 0.5(\nabla \boldsymbol{u}_\infty + (\nabla \boldsymbol{u}_\infty)^T)$ is the rate of strain tensor; and λ is a geometric parameter that is equal to $-1 + 1.5(\ln(8A) - 1.5)/A^2$ for high aspect ratio rings [34], $-1 + 2.24(1 + 0.21\bar{A}^{-0.5})/\bar{A}^{1.5}$ for thin cylindrical disks [35], and $1 - 0.65 \ln(\bar{A})/\bar{A}^2$ for long cylindrical fibers [36]. λ is accurately obtained for rings using boundary element method (BEM) calculations [37].

The analytical solution to Eq. (2.1) is provided by Jeffery in terms of ϕ, the azimuthal angle made by the projection of $\boldsymbol{p}$ in the flow-gradient ($\hat{\boldsymbol{U}}_\infty \hat{\boldsymbol{\Gamma}}_\infty$) plane with the gradient direction of the SSF ($\hat{\boldsymbol{\Gamma}}_\infty$); θ, the polar angle made by $\boldsymbol{p}$ with the vorticity direction ($\hat{\boldsymbol{\Omega}}_\infty$) defined in Fig. 1(a). The analytical solution to Eq. (2.1) is given by

$$\tan(\phi) = \phi_T \tan\left(2\pi \frac{t}{T} + \tau\right), \tag{2.2}$$

$$\tan(\theta) = \frac{C\phi_T}{\sqrt{\phi_T^2 \cos^2(\phi) + \sin^2(\phi)}}, \tag{2.3}$$

where $T = 4\pi/\sqrt{1 - \lambda^2}$ is the time period of rotation; $\phi_T = \sqrt{(1 + \lambda)/(1 - \lambda)} \approx 2\pi/T$ is an effective inverse-aspect ratio; τ is the phase angle; and C is the orbit constant. The leading order value of ϕ_T for a torus is given by $\sqrt{3(\epsilon^{-1} - 1.5)}/(2(\bar{A} - 1))$ [34] where $\epsilon = 1/\ln(8(\bar{A} - 1))$. The time period, T, is $O(\bar{A}\sqrt{\epsilon})$ for rings, $O(\bar{A}^{-0.75})$ for cylindrical disks, $O(\bar{A})$ for oblate spheroids, and $O(\bar{A}\sqrt{\epsilon})$ for fibers [36,35] and is shown in Fig. 1(c).

The orientation trajectories of Eq. (2.1) are closed loops known as Jeffery orbits specified by C and are shown in Fig. 1(b) for an $\bar{A} = 40$ torus. One characteristic of high-aspect ratio rings is that the orbits are pinched near the gradient direction as shown in Fig. 1(b). This orbit pinching implies that $O(1)$ values for angles θ and ϕ correspond to the particle rotating in orbits that have C of $O(\phi_T^{-1})$ or larger. A particle in such an orbit spends a long $O(\phi_T^{-1})$ time aligned close to the flow vorticity plane and performs a quick tumble (i.e., an event where $\boldsymbol{p}$ crosses the flow-vorticity plane) in an $O(1)$ time and repeats this motion periodically. The typical angle made by the plane of a high aspect ratio ring with the flow-vorticity plane during the aligned part of the Jeffery trajectory, also referred to as the tilt of the ring, is $O(\phi_T) = O(\bar{A}\epsilon^{-1})$, which is essentially algebraically small in the aspect ratio $\bar{A}$. The value of ϕ_T will be used throughout this work, and it is important to remember that ϕ_T has a much stronger algebraic scaling with $\bar{A}$ than the logarithmic scaling of the slenderness parameter $\epsilon = 1/\ln(8A)$.

Thus, during a pairwise interaction of two particles, both particles could be in the aligned state; one particle could be aligned and the other tumbling; or both particles could be tumbling. The above events occur with a probability of $O(1)$, $O(\phi_T)$, and $O(\phi_T^2)$ due to the non-uniform Jeffery rotation rate. The mean square change in the particle orientation, $\boldsymbol{p}$, which is proportional to the square of the velocity disturbance and the occurrence frequency of the interaction [24], is a good measure to ascertain the relative importance of each of these interactions. A slender ring generates a much larger $O(\epsilon)$ velocity disturbance during its tumble phase compared to $O(\phi_T \epsilon)$ disturbance produced in its temporarily aligned phase. Using the aforementioned information, the most important pairwise *hydrodynamic interactions* that determine the orientation distribution are between a tumbling and a temporarily aligned torus and these lead to an $O(\epsilon^2 \phi_T)$ mean squared change in $\boldsymbol{p}$. The contribution to the mean square change in $\boldsymbol{p}$ due to pairwise hydrodynamic interactions between two aligned or two tumbling rings is smaller by a factor of $O(\phi_T)$, which is algebraically small in the aspect ratio. Similarly, the most important *collisions* that determine the orientation distribution are between a tumbling and a temporarily aligned ring that lead to an $O(1)$ change in $\boldsymbol{p}$, and this event occurs with a collision frequency of $O(\phi_T)$ [17]. The collision frequency of two aligned or two tumbling tori is $O(\phi_T^2)$ [17]. Thus, an interaction between a tumbling and an aligned ring is the most important pairwise interaction in dilute particle suspensions.

Table I provides a concise list of symbols and their definitions useful while going over the remainder of this section on simulation methodology and Sec. III discussing the results. The reader is encouraged to familiarize with these notations,

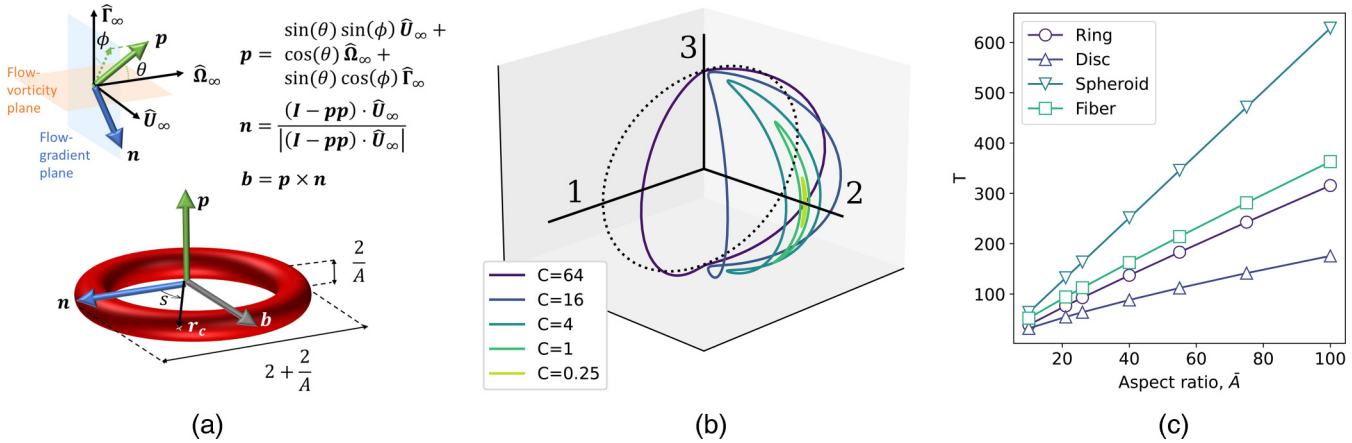

FIG. 1. (a) Fixed coordinate system using the flow ($\hat{\boldsymbol{U}}_\infty$ or 1), vorticity ($\hat{\boldsymbol{\Omega}}_\infty$ or 2), and gradient ($\hat{\boldsymbol{\Gamma}}_\infty$ or 3) directions of the simple shear flow and the definition of the azimuthal (ϕ) and polar (θ) angle of the orientation vector $\boldsymbol{p}$. The particle coordinate system ($\boldsymbol{n}, \boldsymbol{b}, \boldsymbol{p}$) is defined by the orientation vector $\boldsymbol{p}$, the projection of the flow direction of the simple shear flow in the plane of the ring, $\boldsymbol{n} = (\boldsymbol{I}-\boldsymbol{pp})\cdot\hat{\boldsymbol{U}}_\infty/|(\boldsymbol{I}-\boldsymbol{pp})\cdot\hat{\boldsymbol{U}}_\infty|$ and $\boldsymbol{b} = \boldsymbol{p}\times\boldsymbol{n}$, and the origin is chosen as the center of mass of the torus. (b) *Jeffery orbits* of a tumbling torus with $\bar{A} = 40$ with $\lambda = -1 + 4.0\times10^{-3}$ and $\phi_T = 0.045$. The orbit constants plotted are [0.25,1,4,16,64] with the dotted line representing C_∞ orbit ($C \to \infty$). (c) Time period of rotation of rings, cylindrical disks, oblate spheroids, and cylindrical fibers as a function of the particle aspect ratio $\bar{A}$.

particularly the angles (ϕ, θ) describing the orientation vector $\boldsymbol{p}$, the effective inverse aspect ratio ϕ_T, the slenderness parameter ϵ, and the particle aspect ratio $\bar{A}$.

B. Simulation strategy for pairwise interactions of rings

The dilute suspension rheology is calculated by monitoring particle positions, orientations, and stresslet tensors of two rings that are initially widely separated along $\hat{\boldsymbol{U}}_\infty$ for all possible interactions of this two-particle system. The velocity disturbance produced by a rotating ring can be described by a line of Stokeslet singularities placed on the centerline of the ring-cross section in the slender-body-theory (SBT) formulation and the strength of singularities is analytically available [34]. The velocity disturbance computed by SBT is accurate to $O(\epsilon^2)$ when the ring centerlines of two particles (or the particle surfaces) are separated by distances much larger than $\bar{A}^{-1}$. Thus, SBT accurately captures the long-range interactions of two rings [23]. The SBT formulation only breaks down at $O(\bar{A}^{-1})$ separations between centerlines of the two rings wherein a second particle enters the inner region in SBT formulation. However, at such separations, the particle contact driven by the $O(1)$ Jeffery rotation rate and hydrodynamic interactions between more distant portions of the rings dominate over the close-range hydrodynamic interaction, and thus, the inaccuracies of the SBT have negligible effect on the overall dynamics of the two particles [27,8]. Other computational methods such as the boundary element method or a finite-volume-approach would involve an exorbitant amount of computational resources at each time step making them impractical for this calculation.

Consider two particles with orientations $\boldsymbol{p}_I$ and $\boldsymbol{p}_{II}$ and center-of-mass positions $\boldsymbol{r}_{I,COM}$ and $\boldsymbol{r}_{II,COM}$, respectively. An isolated force- and torque-free ring in an SSF translates with the fluid velocity at its center of mass, rotates with Jeffery rotation rate $\dot{\boldsymbol{p}}_J(\boldsymbol{p})$, and exerts an $O(\epsilon)$ force per unit length on the fluid, $\boldsymbol{f}_{SSF}$. The first reflection is the change in the particle velocity, rotation rate, and force distribution caused by the velocity disturbance $\boldsymbol{u}'_\infty$ of a nearby particle. The $O(\epsilon)$ velocity disturbance of the nearby particle induces an additional $O(\epsilon)$ translational velocity $\boldsymbol{U}_{HI}$, an $O(\epsilon)$ angular velocity $\boldsymbol{\omega}_{HI}$, and an $O(\epsilon^2)$ force per unit length $\boldsymbol{f}_{HI} = 4\pi\epsilon(\boldsymbol{U}_{HI} + \boldsymbol{\omega}_{HI}\times(\boldsymbol{r}_c - \boldsymbol{r}_{I,COM}) - \boldsymbol{u}'_\infty)$.

TABLE I. List of symbols and notations describing tumbling motion of rings in a simple-shear-flow (SSF).

Symbol	Description
$\boldsymbol{p}$	Unit vector along the axis of symmetry of the ring
ϕ	Azimuthal angle, the angle between the gradient direction and the projection of $\boldsymbol{p}$ in the flow-gradient plane
θ	Polar angle, the angle between the vorticity direction and the axis-of-symmetry of the ring
$\bar{A}$	Aspect ratio of the ring $\bar{A} = \frac{R}{a} + 1$, where R = ring radius and a = radius of ring cross section
ϵ	$\epsilon = (\ln(8(\bar{A}-1)))^{-1} \ll 1$, slenderness parameter arising in the slender-body-theory treatment of a ring
T	Time period of tumbling in a Jeffery orbit shown in Fig. 1(b)
ϕ_T	Effective inverse aspect ratio of the particle. $\phi_T = \sqrt{(1+\lambda)/(1-\lambda)} \approx 2\pi/T$
C	Jeffery orbit constant lies between 0 and infinity
C_b	$C_b = C/(C+1)$, modified orbit constant that lies between 0 and 1
τ	Phase angle in Jeffery's periodic solution
$\dot{p}_J$	Jeffery rotation rate given by Eq. (2.1)
$\boldsymbol{r}$	Position vector
$\boldsymbol{r}_c$	Position vector describing the centerline of the ring cross section
SSF	Simple-shear-flow
SBT	Slender-body-theory
$\hat{\boldsymbol{U}}_\infty = \hat{\boldsymbol{e}}_1$	Unit vector in the flow direction of SSF
$\hat{\boldsymbol{\Omega}}_\infty = \hat{\boldsymbol{e}}_2$	Unit vector in the vorticity direction of SSF
$\hat{\boldsymbol{\Gamma}}_\infty = \hat{\boldsymbol{e}}_3$	Unit vector in the Gradient direction of SSF
$\boldsymbol{n}$	Projection of the flow direction in the plane of the ring
$\boldsymbol{b}$	$\boldsymbol{b} = \boldsymbol{p}\times\boldsymbol{n}$
$\boldsymbol{e}_z$	Tangent to the ring centerline

$(\boldsymbol{I} - 0.5\,\boldsymbol{e}_z\boldsymbol{e}_z)$ on the fluid. This process of obtaining the velocity disturbance and the corresponding force per unit length can be continued to obtain higher order reflections, the contribution of each subsequent reflection to $\boldsymbol{f}_{HI}$ being smaller by a factor of $O(\epsilon)$. However, the first reflection was deemed sufficient for the problem of determining the effect of hydrodynamic interactions (HI) on the stresslet-tensor for rigid fibers [23,29] and therefore the first reflection alone is retained in this study. The velocity disturbance $\boldsymbol{u}'_\infty$ at $\boldsymbol{r}$ produced by a ring is obtained from a convolution integral over the centerline of the ring cross section given by

$$u'_{\infty,i}(\boldsymbol{r}) = \frac{1}{8\pi}\oint ds\, f_j(\boldsymbol{r}')\left(\frac{\delta_{ij}}{r''} + \frac{r''_i r''_j}{r''^3}\right), \tag{2.4}$$

where ds is the elemental length along the centerline of the ring cross section $\boldsymbol{r}_c$; $\boldsymbol{r}'' = \boldsymbol{r} - \boldsymbol{r}'$, with $\boldsymbol{r}'$ being a position on the centerline of the ring; and $\boldsymbol{f} = \boldsymbol{f}_{SSF} + \boldsymbol{f}_{con}$ and $\boldsymbol{f}_{con}$ is the $O(\epsilon)$ force per unit length induced from particle contact derived shortly. The value of $\boldsymbol{f}_{SSF}$ is obtained from the SBT solution of a single force-and-torque-free ring in an SSF [see Eqs. (S4.6–S4.7) in the supplementary material of [34]]. The values of $\boldsymbol{U}_{HI}$ and $\boldsymbol{\omega}_{HI}$ are obtained by applying the force- and torque-free conditions, respectively. The stresslet tensor associated with $\boldsymbol{f}_{HI}$ is given by

$$\boldsymbol{S}_f = \oint ds\, \left(\frac{(\boldsymbol{f}_{HI}\boldsymbol{r}_c + \boldsymbol{r}_c\boldsymbol{f}_{HI})}{2} - (\boldsymbol{r}_c \cdot \boldsymbol{f}_{HI})\frac{\boldsymbol{I}}{3}\right), \tag{2.5}$$

where the path integral is performed along $\boldsymbol{r}_c$.

In addition to HI, collision of two tumbling rings is also important at dilute concentrations. The lubrication force between nearly touching high-aspect ratio rings is qualitatively similar to the lubrication force between two colliding cylinders, which is $O(\dot{\delta}/(\bar{A}^2\delta))$ [38], with δ being the distance of minimum separation between the cylinders and $\dot{\delta}$ is the rate of change of δ. The stresses due to the SSF driving the two rings together act over the entire length of the particle, and therefore, the contact force must be $O(1)$. Harlen and coworkers [39] argued that in an $O(1)$ time δ changes by a factor of $\exp(-\bar{A}^2)$, which for practical purposes implies a solid body contact between high-aspect ratio cylinders. Two rings that are about to collide, which would have local forces similar to two contacting cylinders, should, therefore, also make mechanical contact.

The collision event near the point of contact is simulated by applying a short-range repulsive force, $\boldsymbol{F}_{con}$, that prevents particles from passing through each other and depends only on the distance of minimum separation of the tori surface δ. $\boldsymbol{F}_{con}$ acts on one or two points on the rings, and the latter case could happen when one ring enters the hole of the other ring or when rings are parallel to each other. The functional dependence of $\boldsymbol{F}_{con}$ on δ was chosen to be similar to $\boldsymbol{F}_{con}$ used to simulate collision of two disks by Meng and Higdon (2008) [10] and is given by

$$\boldsymbol{F}_{con} = 8\pi C_p \frac{\delta_{min}}{\delta}\left(\eta - \frac{\eta^2}{2}\right)^3 \boldsymbol{d}\,, \tag{2.6}$$

where $\eta = 1 - \delta/\delta_{min}$, $\boldsymbol{d}$ is a unit vector normal to the collision surface at the point of the closest approach and points toward the centerline of the particle experiencing the force, and C_p is an $O(1)$ constant. Values of C_p between 10^2 and 10^3 provided results that were insensitive to the choice C_p in a reasonable computational time per trajectory. The exact functional form of $\boldsymbol{F}_{con}$ with δ is known to have no effect on the overall dynamics and suspension rheology as long as it is steep and the force acts for $\delta_{min} \le O(A^{-1})$ [26,20,9]. δ_{min} was chosen to be $10^{-2}A^{-1}$, and $\boldsymbol{F}_{con}$ is limited to a maximum value corresponding to $\delta = 10^{-2}\delta_{min}$ for all our simulations to prevent the time step from becoming extremely small. Less than about 0.1% of our simulations prematurely terminated because of restricting the magnitude of the contact force.

The point of contact is first estimated by discretizing the centerline of the two rings into N^* elements each of length $2\pi/N^* = O(A^{-1})$ as shown in Fig. 2(a) and searching for two elements on each ring with the two lowest values of $|\boldsymbol{r}^i_{C,I} - \boldsymbol{r}^j_{C,II}|$, where $\boldsymbol{r}^i_{C,I}$ and $\boldsymbol{r}^j_{C,II}$ are the centers of the elements on the two ring centerlines. The elements with minimum separation obtained from the previous search $(\boldsymbol{r}^*_{C,I}, \boldsymbol{r}^*_{C,II})$ are further discretized into N^{**} smaller elements ($N^{**} = N^* = 200$ was chosen in all our simulations) to compute the separation distance more accurately as shown in Fig. 2(a). $\boldsymbol{F}_{con}$ is applied at the centerline of the ring cross section instead of the exact point of contact, which only creates errors of $O(\bar{A}^{-2})$ in the computation of the angular velocity.

The linear ($\boldsymbol{U}_{con}$) and angular ($\boldsymbol{\omega}_{con}$) velocities of the particle due to contact obtained by applying the force and torque-free condition on the particle, respectively, are

$$\boldsymbol{U}_{con} = \frac{1}{6\pi^2\epsilon(1-A^{-1})^2}\sum_{k=1}^{2}\boldsymbol{F}^k_{con} \cdot \left(\frac{1-\frac{17}{6}\epsilon}{1-\frac{5}{2}\epsilon-\epsilon^2}(\boldsymbol{I}-\boldsymbol{pp}) + \frac{3}{4}\frac{1}{1+\frac{\epsilon}{2}}\boldsymbol{pp}\right), \tag{2.7}$$

$$\boldsymbol{\omega}_{con} = \frac{1}{4\pi^2\epsilon(1-A^{-1})^3}\sum_{k=1}^{2}\left(\left(\boldsymbol{r}^k_{c,con} - \boldsymbol{r}_{COM}\right)\times\boldsymbol{F}^k_{con}\right) \cdot \left(\frac{\boldsymbol{I}-\boldsymbol{pp}}{1-1.5\epsilon} + \frac{\boldsymbol{pp}}{1-2\epsilon}\right), \tag{2.8}$$

where $\boldsymbol{r}^k_{c,con}$ are the two points of contact for the particle and $\boldsymbol{r}_{COM}$ is the center of mass of the ring [31]. The contact induces an $O(\epsilon)$ force per unit length $\boldsymbol{f}_{con}$, which is given by $\boldsymbol{f}_{con} = 4\pi\epsilon(\boldsymbol{U}_{con} + \boldsymbol{\omega}_{con}\times(\boldsymbol{r}_c - \boldsymbol{r}_{I,COM}))\cdot(\boldsymbol{I} - 0.5\,\boldsymbol{e}_z\boldsymbol{e}_z)$. $\boldsymbol{f}_{con}$ needs to be included while computing the velocity disturbance in Eq. (2.4) and is important when particles collide. Particle contact also induces a stresslet $\boldsymbol{S}_{con}$ that is given by

$$\boldsymbol{S}_{con} = -\frac{1}{2}\left(\frac{(\boldsymbol{r}_{CI} - r_{CII})\boldsymbol{F}_{con} + \boldsymbol{F}_{con}(\boldsymbol{r}_{CI} - r_{CII})}{2} - \frac{1}{3}((\boldsymbol{r}_{CI} - r_{CII})\cdot\boldsymbol{F}_{con})\boldsymbol{I}\right). \tag{2.9}$$

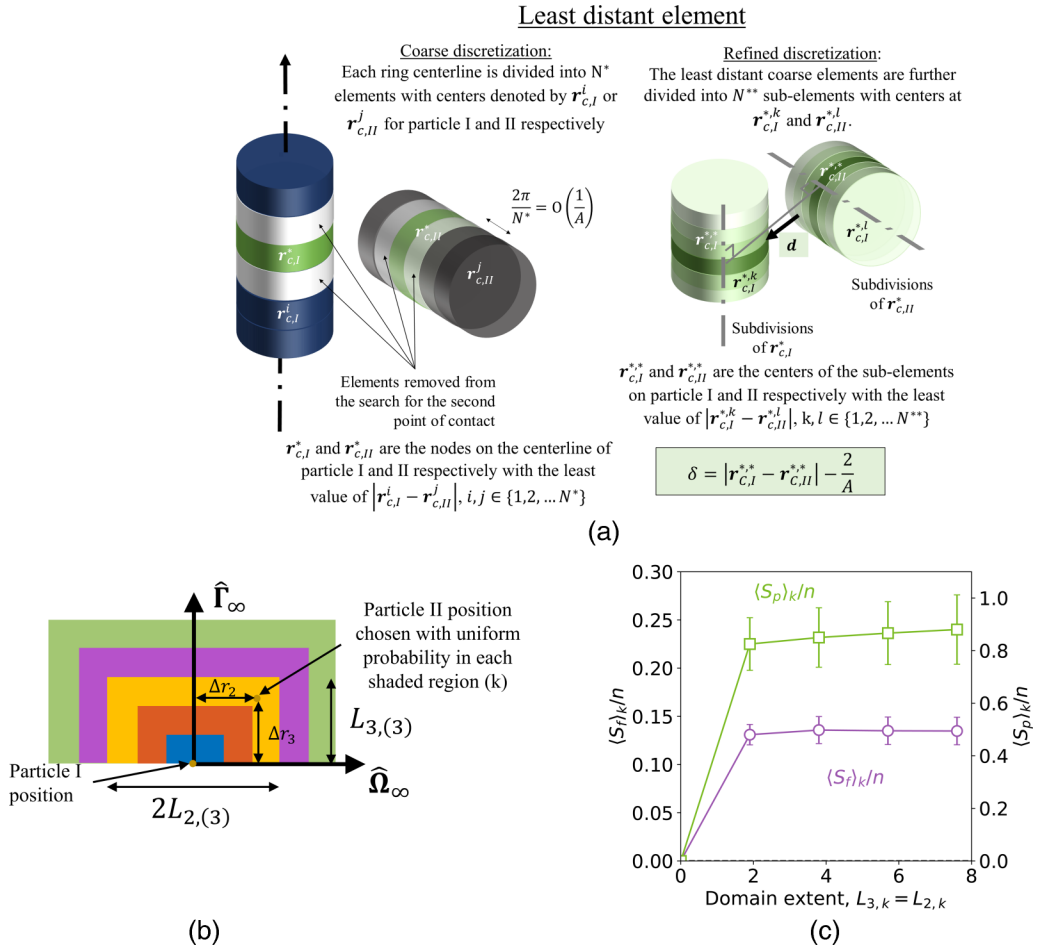

FIG. 2. (a) Discretization of the centerline of each ring into N^* segments to detect the minimum distance between the particles, δ, and the direction of the contact force $\boldsymbol{d}$ (shown for particle I). The segments neighboring the closest segments from coarse discretization are removed while searching for a possible second point of contact of the rings. This algorithm is turned on only when $|\boldsymbol{r}_{I,COM} - \boldsymbol{r}_{II,COM}| \leq 2$. (b) Discretization of the vorticity-gradient plane into multiple regions for computing ensemble average particle properties according to Eq. (2.10). The extent of each subsequent region is increased by two units compared to the previous region in the $\hat{\boldsymbol{\Omega}}_\infty \hat{\boldsymbol{\Gamma}}_\infty$ plane. In the streamwise direction, the starting position is $\Delta \boldsymbol{r}_i \cdot \hat{\boldsymbol{U}}_\infty = 80 L_{3,(j)}$ and the ending position is $\Delta \boldsymbol{r}_f \cdot \hat{\boldsymbol{U}}_\infty = 240 L_{3,(j)}$. (c) Convergence of $\langle S_f \rangle$ and $\langle S_p \rangle$, the contributions to the shear stress from $\boldsymbol{f}_{HI}$ and the transient change in the $\boldsymbol{p}$ during the PI respectively, as a function of the domain size $L_{2,k} = L_{3,k}$ using the renormalization procedure in Sec. II C.

Although collisions involve short-range interactions, $\boldsymbol{S}_{con}$ is $O(\epsilon)$, being asymptotically larger than the $O(\epsilon^2)$ stresslet of $\boldsymbol{S}_f$ due to the velocity disturbance produced by HIs.

The particle positions and orientations are obtained by solving a set of ordinary differential equations given by

$$\frac{d\boldsymbol{r}_{k,\ COM}}{dt} = \boldsymbol{u}_\infty(\boldsymbol{r}_{k,COM}) + \boldsymbol{U}_{HI} + \boldsymbol{U}_{col}, \tag{2.10}$$

$$\frac{d\boldsymbol{p}_k}{dt} = \boldsymbol{p}_k \cdot \boldsymbol{R}_\infty + \lambda(\boldsymbol{E}_\infty \cdot \boldsymbol{p}_k - \boldsymbol{E}_\infty : \boldsymbol{p}_k \boldsymbol{p}_k \boldsymbol{p}_k) + (\boldsymbol{\omega}_{HI} + \boldsymbol{\omega}_{col}) \times \boldsymbol{p}_k, \tag{2.11}$$

where $k = \{I, II\}$ are indices of the two particles and $\boldsymbol{u}_\infty(\boldsymbol{r}) = \boldsymbol{r} \cdot \hat{\boldsymbol{\Gamma}}_\infty \hat{\boldsymbol{U}}_\infty$ is the imposed shear flow. The Runge–Kutta method with adaptive time stepping is used to march forward in time. The maximum time step in the simulation was restricted to $0.1\,\bar{A}^{-1}$ to ensure that the particle contact events are not missed during simulation.

The ensemble average value of a particle property of interest $\boldsymbol{X}$ per unit concentration due to pairwise interactions (PIs) (i.e., $\langle \boldsymbol{X} \rangle_{PI}/n$) is evaluated from the flux of the time integral of $\boldsymbol{X}$ relative to the value resulting from Jeffery rotation, passing through the $\hat{\boldsymbol{\Omega}}_\infty - \hat{\boldsymbol{\Gamma}}_\infty$ plane [40] and averaged over the steady state orientation distribution of the two particles. The value of $\langle \boldsymbol{X} \rangle_{PI}/n$ is mathematically given by

$$\frac{\langle \boldsymbol{X} \rangle_{PI}}{n} = \oint_{\hat{\boldsymbol{\Omega}}_\infty - \hat{\boldsymbol{\Gamma}}_\infty} dA\ (\Delta \boldsymbol{r}_0) \cdot \hat{\boldsymbol{\Gamma}}_\infty \int dC_b^I\, p(C_b^I) \int \frac{d\tau_I}{2\pi} \int dC_b^{II}\, p(C_b^{II}) \times \int \frac{d\tau_{II}}{2\pi} \int_{-\infty}^{\infty} dt\ (\boldsymbol{X}(t) - \boldsymbol{X}_J(t)), \tag{2.12}$$

where $i \in \{I, II\}$ are the indices for the two particles in the simulation; $\boldsymbol{X}_J$ is the value of $\boldsymbol{X}$ evaluated in the absence of a second particle and $p(C_b)$ is the steady state probability distribution of the modified orbit constant $C_b = C/(C+1)$, which is discussed in Sec. II D. Monte-Carlo summation is used to evaluate the integral instead of integrating over the six

degrees of freedom in Eq. (2.12), and the expression for the average quantity simplifies to

$$\frac{\langle \boldsymbol{X} \rangle_{PI}}{n} = \sum_j \frac{A_j}{N_j} \sum_{k=1}^{N_j} (\Delta \boldsymbol{r}_0)_k \cdot \hat{\boldsymbol{\Gamma}}_\infty \int_{-\infty}^{\infty} dt \, (\boldsymbol{X}_k(t) - \boldsymbol{X}_{J,k}(t)) = \sum_j A_j \sum_{k=1}^{N_j} \frac{I_k}{N_j}, \tag{2.13}$$

where I_k is equal to the product of the time integral and the relative velocity of the particles, A_j is the area of the jth region in the gradient-vorticity plane in which the points are chosen with uniform probability as shown in Fig. 2(b), $(\Delta \boldsymbol{r}_0)_k \cdot \hat{\boldsymbol{\Gamma}}_\infty$ is a weighting function proportional to the flux of the particles per unit concentration flowing across the vorticity-gradient plane and $\Delta \boldsymbol{r}_0$ is initial separation between the center of mass of the two particles. The flow-vorticity plane is split into multiple regions of areas A_j as shown in Fig. 2(b) to establish convergence of relevant particle properties such as orientational dispersion, hydrodynamic diffusivity and the stresslet tensor with increasing phase-space of initial cross-stream positions in a systematic fashion. The initial positions of the center of mass of the two particles were chosen to be $\boldsymbol{r}_{I,COM} = 0$ and $\boldsymbol{r}_{II,COM} = \Delta \boldsymbol{r}_0$. The initial orientations $\boldsymbol{p}_{I,0}$ and $\boldsymbol{p}_{II,0}$ are specified in terms of the phase angles (τ_I, τ_{II}) chosen uniformly between $[0, 2\pi)$ and the orbit constants (C_I, C_{II}) chosen from the steady state orbit distribution discussed in Sec. II D. $\Delta \boldsymbol{r}_0 \cdot \hat{\boldsymbol{\Gamma}}_\infty$ was chosen with a uniform probability between $[0, L_3)$ and $\Delta \boldsymbol{r}_0 \cdot \hat{\boldsymbol{\Omega}}_\infty$ was chosen with a uniform probability from $[-L_2, L_2]$. The value of $\Delta \boldsymbol{r}_0 \cdot \hat{\boldsymbol{U}}_\infty \geq -80L_3$ simulates an initial large separation between the two particles. The simulation is run until $\Delta \boldsymbol{r} \cdot \hat{\boldsymbol{U}}_\infty = 240L_3$, which is a sufficiently large distance to reduce the influence of interparticle interactions. This strategy ensures that the tails of the time integral in Eq. (2.13) (as $t \to \pm\infty$) have an insignificant contribution to $\langle \boldsymbol{X} \rangle_{PI}$. The mean of most quantities of interest for regions with $(L_2, L_3) \geq (8, 8)$ is less than 5% of the value in region with $(L_2, L_3) = (2, 2)$. Only the translational diffusivity calculations described later required calculations from regions as large as $(L_2, L_3) = (16, 16)$. The statistical error in the stresses in regions with $(L_2, L_3) \geq (16, 16)$ was comparable to the mean after 2×10^4 Monte-Carlo simulations and $O(1/\sqrt{N})$ scaling would require at least one hundred times more calculations, which are beyond the scope of this study. $(2-4) \times 10^4$ PI simulations were found to be sufficient to reach a statistically convergent mean value. The standard deviation of the inner summation $\sigma_{I,j}$ for the jth region is given by

$$\sigma_{I,j}^2 = \frac{1}{N_j} \sum_{k=1}^{N_j} \left(I_k - \sum_{k=1}^{N_j} \frac{I_k}{N_j} \right)^2. \tag{2.14}$$

The expression for $\langle \boldsymbol{X} \rangle_{PI}$ with the standard error within 95% confidence limits is given by

$$\frac{\langle \boldsymbol{X} \rangle_{PI}}{n} = \sum_j A_j \left\{ \frac{1}{N_j} \sum_{k=1}^{N_j} I_k \pm 1.96 \, \frac{\sigma_{I,j}}{\sqrt{N_j}} \right\}. \tag{2.15}$$

PIs lead to a transient change in the orientation vector $\boldsymbol{p}$ relative to the Jeffery rotation whose effects on suspension-averaged orientational dispersion can be quantified by the tensor $\langle \boldsymbol{pp} \rangle = \langle \boldsymbol{pp} \rangle_J + n(\langle \boldsymbol{pp} \rangle / n)$. Here, $\langle \rangle_J$ refers to an ensemble average of $\boldsymbol{pp}$ for isolated particles undergoing Jeffery rotation with the steady state orbit distribution and $\langle \rangle$ corresponds to contribution from the transient change in the value of $\boldsymbol{pp}$ from $\langle \boldsymbol{pp} \rangle_J$ during a PI. The value of $\langle \boldsymbol{pp} \rangle$ is calculated by the equation given by

$$\frac{\langle \boldsymbol{pp} \rangle}{n} = \sum_j \frac{A_j}{N_j} \sum_{k=1}^{N_j} (\Delta \boldsymbol{r}_0)_k \cdot \hat{\boldsymbol{\Gamma}}_\infty \int_{-\infty}^{\infty} dt [\boldsymbol{p}(t)\boldsymbol{p}(t) - \boldsymbol{p}_J(t, \tau_i, C_i) \, \boldsymbol{p}_J(t, \tau_i, C_i)(1 - H(t - t_{HI})) - \boldsymbol{p}_J(t, \tau_f, C_f) \, \boldsymbol{p}_J(t, \tau_f, C_f) H(t - t_{HI})], \tag{2.16}$$

where $\boldsymbol{p}_J$ is the orientation defined by Eqs. (2.1)–(2.3); $H(t - t_{HI})$ is the Heaviside step-function; $t_{HI} = (\Delta \boldsymbol{r}_0) \cdot \hat{\boldsymbol{U}}_\infty / (\Delta \boldsymbol{r}_0) \cdot \hat{\boldsymbol{\Gamma}}_\infty$; C_i, τ_i and C_f, τ_f are the (orbit constant, phase angle) before $(t \to -\infty)$ and after the interaction $(t \to +\infty)$, respectively. The choice of the time for shifting from (C_i, τ_i) to (C_f, τ_f) in Eq. (2.13) is arbitrary but was chosen to be at the location near $\Delta \boldsymbol{r} \cdot \hat{\boldsymbol{U}}_\infty = 0$ to reduce statistical errors in the summation. The particle interaction on average should be strongest close to $(\Delta \boldsymbol{r}) \cdot \hat{\boldsymbol{U}}_\infty = 0$ and the change in the orbit constant should be greatest near this separation. The distribution of orbit constants of all trajectories after interactions must be the same as the initial steady state orbit distribution. The mean of the orbit constant over MC simulations in each region-k before and after the interaction differed by less than 1% in all our simulations. Equation (2.16) requires a renormalization procedure that is discussed in Sec. II C. Equation (2.16) can be extended for other moments of orientation as well.

In addition to orientation dispersion, particle centers also drift away from their original streamline in dilute suspension during particle encounters. This drifting motion across many different particle interactions is diffusive in nature [41,40] and can be characterized by translational diffusion coefficients in the gradient (D_{33}) and vorticity (D_{22}) direction which on simplifying Eq. (2.13) is given by

$$\frac{D_{22}}{n} = \frac{1}{2} \sum_j \frac{A_j}{N_j} \sum_{k=1}^{N_j} (\Delta \boldsymbol{r}_0)_k \cdot \hat{\boldsymbol{\Gamma}}_\infty \left(((\boldsymbol{r}_\infty)_k - (\boldsymbol{r}_0)_k) \cdot \hat{\boldsymbol{\Omega}}_\infty \right)^2, \tag{2.17}$$

$$\frac{D_{33}}{n} = \frac{1}{2} \sum_j \frac{A_j}{N_j} \sum_{k=1}^{N_j} (\Delta \boldsymbol{r}_0)_k \cdot \hat{\boldsymbol{\Gamma}}_\infty \left(((\boldsymbol{r}_\infty)_k - (\boldsymbol{r}_0)_k) \cdot \hat{\boldsymbol{\Gamma}}_\infty \right)^2. \tag{2.18}$$

Here, $(\boldsymbol{r}_\infty)_k \cdot \hat{\boldsymbol{\Omega}}_\infty$ and $(\boldsymbol{r}_\infty)_k \cdot \hat{\boldsymbol{\Gamma}}_\infty$ are the separation of the center of mass of the kth particle in vorticity and gradient directions after the interaction (i.e., when $(\Delta \boldsymbol{r})_k \cdot \hat{\boldsymbol{U}}_\infty \to +\infty$).

Table II provides a summary of major definitions used in this section, particularly, the different contributions to the force-per-unit length, particle velocities, and the ensemble average of particle properties due to pairwise interactions.

TABLE II. List of symbols for simulating the dynamic change in the particle position, orientation, and stresslet tensor during pairwise interaction (PI) with other rings.

Symbol	Description
$\boldsymbol{f}_{SSF}$	Force per unit lengtd on tde centerline of a torque and force free torus tumbling in a simple shear flow
$\boldsymbol{f}_{con}$	Force per unit length on the ring centerline arising from contact forces
$\boldsymbol{S}_{con}$	Stresslet tensor associated with the contact force
$\boldsymbol{u}'_{\infty}$	Velocity disturbance produced by neighboring ring due to ($\boldsymbol{f}_{SSF}+\boldsymbol{f}_{con}$) given by Eq. (2.4)
$\boldsymbol{f}_{HI}$	Force per unit length on the ring centerline from the velocity disturbance of a neighboring ring $\boldsymbol{u}'_{\infty}$
$\boldsymbol{S}_{f}$	Stresslet tensor associated with $\boldsymbol{f}_{HI}$
($\boldsymbol{U}_{con}$, $\boldsymbol{\omega}_{con}$)	Linear and angular velocity driven by contact forces
($\boldsymbol{U}_{HI}$, $\boldsymbol{\omega}_{HI}$)	Linear and angular velocity caused by $\boldsymbol{u}'_{\infty}$
$\boldsymbol{r}_{k,\ COM}$	Center-of-mass position of particle-k
n	Number density non-dimensionalized by R^{-3} where R is the ring radius
$\langle\rangle$	Ensemble average of contributions to particle properties from all possible realization of pairwise particle interactions
$\Delta\boldsymbol{r}_0$	Initial separation of the center of mass of particle-II relative to the center of mass of particle-I
(C_i, τ_i)	Initial orbit constant and phase angle of the Jeffery tumbling trajectory
(C_f, τ_f)	Final orbit constant and phase angle of the Jeffery tumbling trajectory
$\langle\rangle_J$	Ensemble average of particle properties averaged over the steady-state orbit distribution and Jeffery rotation rate
A_j	Area of the jth region in the vorticity-gradient plane with locations of the initial relative positions of the particles as shown in Fig. 2(b)
LH	Leal and Hinch orbit distribution
D_{ii}	Translational diffusivity of particles in the vorticity ($i=2$) and gradient ($i=3$) direction of the SSF

Overall, the calculations derived in this subsection capture transient deviations in the particle position, orientation, and stresslet from the values associated with Jeffery rotation across all possible interactions of the two-particle system.

C. Stresslet evaluation

A particle exerts stresses on the fluid thereby changing the rheological behavior of the corresponding suspension. This change in rheology can be expressed in terms of the stresslet tensor $\boldsymbol{S}$ equal to the symmetric part of the first moment of the stress acting on the particle surface and is computed from a surface integral given by

$$\boldsymbol{S}=\int dA\left(\frac{\boldsymbol{r}(\boldsymbol{\sigma}\cdot\tilde{\boldsymbol{n}})+(\boldsymbol{\sigma}\cdot\tilde{\boldsymbol{n}})\boldsymbol{r}}{2}-\frac{\boldsymbol{\sigma}:\tilde{\boldsymbol{n}}\boldsymbol{r}}{3}\boldsymbol{I}\right), \tag{2.19}$$

where $\boldsymbol{\sigma}=-p\,\boldsymbol{I}+(\nabla\boldsymbol{u}+(\nabla\boldsymbol{u})^{T})$ is the stress tensor, $\boldsymbol{u}$ is the velocity field in the presence of particles, $\tilde{\boldsymbol{n}}$ is the outward unit normal to the surface, $\boldsymbol{r}$ is the position vector, and dA is the elemental area on the particle surface. A single particle contribution to the stresslet tensor arising from Jeffery rotation is discussed before deriving the ensemble average equations for the $O(n)$ correction to the stresslet tensor arising from PIs.

The velocity field $\boldsymbol{u}$ and pressure p can be approximated from the complete inner solution of the SBT as $\boldsymbol{u}_{inner}$ and p_{inner} for an isolated ring. The instantaneous stresslet of an isolated axisymmetric particle, $\boldsymbol{S}_{Hyd}$, in a simple shear flow can be expressed in terms of $\boldsymbol{E}_{\infty}$ and moments of $\boldsymbol{p}$ and is given by

$$\begin{aligned}\boldsymbol{S}_{Hyd}=\xi_1\boldsymbol{E}_{\infty}\ &+\xi_2\left(\boldsymbol{E}_{\infty}\cdot\boldsymbol{pp}+\boldsymbol{pp}\cdot\boldsymbol{E}_{\infty}-\frac{2}{3}\boldsymbol{pp}:\boldsymbol{E}_{\infty}\boldsymbol{I}\right)\\&+\xi_3\left(\boldsymbol{E}_{\infty}:\boldsymbol{pppp}-\frac{1}{3}\boldsymbol{pp}:\boldsymbol{E}_{\infty}\boldsymbol{I}\right),\end{aligned} \tag{2.20}$$

where ξ_i for $i=\{1,2,3\}$ are $O(\epsilon)$ constants that depend only on the particle shape, with $\xi_1+\xi_2=O(A^{-2})$ [42]. ξ_i are obtained using SBT (see Appendix A1), instead of BEM calculations, to remain consistent with additional $O(n^2)$ stresslet tensor contributions computed during PIs using the SBT framework. The SBT values for ξ_i are in good agreement with the exact values obtained from BEM for the aspect ratios considered in this study (see Fig. 9 in the Appendix). Equation (2.20) provides insight into the anisotropic change in the suspension stress due to the presence of noninteracting rigid particles. The ensemble average stresslet tensor, $\langle\boldsymbol{S}_{Hyd}\rangle_J$, which is the value of $\boldsymbol{S}_{Hyd}$ averaged over Jeffery trajectories and the steady state orbit distribution, is given by

$$\begin{aligned}\langle\boldsymbol{S}_{Hyd}\rangle_J=\xi_1\boldsymbol{E}_{\infty}+&+\xi_2\left(\boldsymbol{E}_{\infty}\cdot\langle\boldsymbol{pp}\rangle_J+\langle\boldsymbol{pp}\rangle_J\cdot\boldsymbol{E}_{\infty}-\frac{2}{3}\boldsymbol{E}_{\infty}:\langle\boldsymbol{pp}\rangle_J\,\boldsymbol{I}\right)\\&+\xi_3\left(\boldsymbol{E}_{\infty}:\langle\boldsymbol{pppp}\rangle_J-\frac{1}{3}\boldsymbol{E}_{\infty}:\langle\boldsymbol{pp}\rangle_J\boldsymbol{I}\right).\end{aligned} \tag{2.21}$$

The intrinsic viscosity is proportional to the $\hat{\boldsymbol{\Gamma}}_{\infty}\hat{\boldsymbol{U}}_{\infty}$ component of this tensor.

PIs between particles lead to additional contributions to particle stresses. The stresslet tensor in a dilute suspension of rings can be expressed as $\langle\boldsymbol{S}_{Hyd}\rangle_J+n\left(\langle\boldsymbol{S}_p\rangle/n+\langle\boldsymbol{S}_f\rangle/n+\langle\boldsymbol{S}_{con}\rangle/n\right)$, where $\langle\boldsymbol{S}_p\rangle$ is the ensemble average value of $\boldsymbol{S}_{Hyd}$ relative to $\langle\boldsymbol{S}_{Hyd}\rangle_J$ driven by transient changes in $\boldsymbol{p}$ during PIs with other rings in the suspension; $\langle\boldsymbol{S}_f\rangle$ is the ensemble average of the stresslet induced by velocity disturbances imparted by other particles in the suspension; and $\langle\boldsymbol{S}_{con}\rangle$ is the ensemble average of the stresslet imparted by particle contact forces. The terms $\langle\boldsymbol{S}_p\rangle$, $\langle\boldsymbol{S}_f\rangle$, and $\langle\boldsymbol{S}_{con}\rangle$ are all proportional to n.

The contribution, $\langle\boldsymbol{S}_p\rangle$, accounts for the transient change in the particle orientation $\boldsymbol{p}$ from its Jeffery trajectory as it interacts with various particles in the suspensions and is mathematically expressed as

$$\frac{\langle \boldsymbol{S}_p \rangle}{n} = \sum_j \frac{\langle \boldsymbol{S}_p \rangle_j}{n} = \sum_j \frac{A_j}{N_j} \sum_{k=1}^{N_j} (\Delta \boldsymbol{r}_0)_k \cdot \hat{\boldsymbol{\Gamma}}_\infty \int_{-\infty}^{\infty} dt [\boldsymbol{S}_{Hyd}(\boldsymbol{p}) - \boldsymbol{S}_{Hyd}(\boldsymbol{p}_J(t, \tau_i, C_i))(1 - H(t - t_{HI})) - \boldsymbol{S}_{Hyd}(\boldsymbol{p}_J(t, \tau_f, C_f))H(t - t_{HI})]. \quad (2.22)$$

In addition to the indirect contribution to the average stresslet, there is a more direct contribution from $\boldsymbol{f}_{HI}$ and $\boldsymbol{f}_{con}$ (or equivalently the contact force $\boldsymbol{F}_{con}$) as described by Eqs. (2.5) and (2.9), respectively. The value of $\langle \boldsymbol{S}_f \rangle$ is given by

$$\frac{\langle \boldsymbol{S}_f \rangle}{n} = \sum_j \frac{\langle \boldsymbol{S}_f \rangle_j}{n} = \sum_j \frac{A_j}{N_j} \sum_{k=1}^{N_j} (\Delta \boldsymbol{r}_0)_k \cdot \hat{\boldsymbol{\Gamma}}_\infty \int_{-\infty}^{\infty} dt\, \boldsymbol{S}_f, \quad (2.23)$$

and $\langle \boldsymbol{S}_{con} \rangle$ is given by

$$\frac{\langle \boldsymbol{S}_{con} \rangle}{n} = \sum_j \frac{A_j}{N_j} \sum_{k=1}^{N_j} (\Delta \boldsymbol{r}_0)_k \cdot \hat{\boldsymbol{\Gamma}}_\infty \int_{-\infty}^{\infty} dt\, \boldsymbol{S}_{con}. \quad (2.24)$$

Equations (2.22) and (2.23) lead to nonconvergent area integrals over the $\hat{\boldsymbol{\Gamma}}_\infty - \hat{\boldsymbol{\Omega}}_\infty$ plane because $\boldsymbol{S}_f$ and $\boldsymbol{S}_p$ scale with Δr^{-3}; Δr being the relative distance between the particles. The nonconvergence of $\boldsymbol{S}_f$ can be removed by adopting the renormalization strategy used for obtaining the $O(n^2)$ correction to the viscosity of spheres [43]. A term $\int_{-\infty}^{\infty} dt\, \boldsymbol{S}_f^{RN}$ where $\boldsymbol{S}_f^{RN}$ has the same Δr^{-3} decay behavior as $\boldsymbol{S}_f$ but has zero ensemble average is subtracted from the inner summation of Eq. (2.20), thereby leading to an integrand that decays as Δr^{-6} and a rapidly convergent integral. The term $\boldsymbol{S}_f^{RN}$ is the stresslet associated with the force per unit length $\boldsymbol{f}_{HI}^{RN}$ on particle I due to the mean velocity disturbance produced by a uniform suspension of noninteracting rings. The ensemble average of $\boldsymbol{S}_f^{RN}$ is zero as the mean velocity disturbance over all particles in the suspension is zero. The value of $\boldsymbol{S}_f^{RN}$ is numerically computed from the stresslet contribution of $\boldsymbol{f}_{HI}^{RN}$ as two noninteracting rings move past each other. This ensemble average is computed for each initial condition in the original calculation to reduce the statistical errors in the Monte Carlo summation. The renormalized equation for evaluating $\langle \boldsymbol{S}_f \rangle$ is given by

$$\frac{\langle \boldsymbol{S}_f \rangle}{n} = \sum_j \frac{\langle \boldsymbol{S}_f \rangle_j}{n} = \sum_j \frac{A_j}{N_j} \sum_{k=1}^{N_j} (\Delta \boldsymbol{r}_0)_k \cdot \hat{\boldsymbol{\Gamma}}_\infty \int_{-\infty}^{\infty} dt\, \left(\boldsymbol{S}_f - \boldsymbol{S}_f^{RN}\right). \quad (2.25)$$

The Δr^{-3} parts of $\boldsymbol{S}_f$ and $\boldsymbol{S}_f^{RN}$ exactly cancel for $\Delta r \gg 1$ leading to a rapidly convergent summation. The value of $\langle S_f \rangle / n$, $\langle S_f \rangle = \langle \boldsymbol{S}_f \rangle : \hat{\boldsymbol{\Gamma}}_\infty \hat{\boldsymbol{U}}_\infty$, computed using (2.25) is shown in Fig. 2(c) as a function of the maximum extent over which the summation is performed. The renormalized equations converge rapidly to the steady state value within the region corresponding to $(L_2, L_3) = (1.9, 1.9)$. Only the component contributing to the shear stress of the suspension needs renormalization as trajectories with purely hydrodynamic interactions cannot generate normal stresses [27]. Normal stresses can, therefore, be calculated using Eqs. (2.22)–(2.24) by taking the contribution from contacting trajectories alone.

The renormalization procedure for $\boldsymbol{S}_p$ involves using the influence of a set of particles in the suspension not perturbed by particle I, similar to the previous renormalization procedure for $\boldsymbol{S}_f$. First a linearized transient change in $\boldsymbol{p}$ relative to its Jeffery trajectory $\boldsymbol{p}_J$, termed $\Delta \boldsymbol{p} = \boldsymbol{p} - \boldsymbol{p}_J$, is computed from the velocity disturbance produced by the set of particles tumbling in Jeffery orbits and translating with the shear flow velocity at its center of mass. Then a term $\Delta \boldsymbol{S}_{Hyd}^{RN}(\Delta \boldsymbol{p}, \boldsymbol{p}_J)$ that is the $O(\Delta \boldsymbol{p})$ term in the Taylor expansion of $\boldsymbol{S}_{Hyd}(\boldsymbol{p}) - \boldsymbol{S}_{Hyd}(\boldsymbol{p}_J)$ is computed, which has the same Δr^{-3} decay as $\boldsymbol{S}_{Hyd}(\boldsymbol{p}) - \boldsymbol{S}_{Hyd}(\boldsymbol{p}_J)$ for the original calculation at $\Delta r \gg 1$. Subtracting the time integrals of $\Delta \boldsymbol{S}_{Hyd}^{RN}(\Delta \boldsymbol{p}, \boldsymbol{p}_J)$ from the time integral of $\boldsymbol{S}_{Hyd}(\boldsymbol{p}) - \boldsymbol{S}_{Hyd}(\boldsymbol{p}_J)$ provides a converging summation. $\Delta \boldsymbol{S}_{Hyd}^{RN}(\Delta \boldsymbol{p}, \boldsymbol{p}_J)$ is the stresslet produced by the gradient in the velocity disturbance of a suspension of rings tumbling in Jeffery orbits. The ensemble average value of $\Delta \boldsymbol{S}_{Hyd}^{RN}(\Delta \boldsymbol{p}, \boldsymbol{p}_J)$ is zero because rings tumbling in Jeffery orbits produce zero-average velocity gradient.

The value of $\Delta \boldsymbol{S}_{Hyd}^{RN}$ is given by

$$\Delta \boldsymbol{S}_{Hyd}^{RN}(\Delta \boldsymbol{p}, \boldsymbol{p}_J) = \xi_2 \Big(\boldsymbol{E}_\infty \cdot (\boldsymbol{p}_J \Delta \boldsymbol{p} + \Delta \boldsymbol{p} \boldsymbol{p}_J) + (\boldsymbol{p}_J \Delta \boldsymbol{p} + \Delta \boldsymbol{p} \boldsymbol{p}_J) \cdot \boldsymbol{E}_\infty - \frac{2}{3} \boldsymbol{E}_\infty : (\boldsymbol{p}_J \Delta \boldsymbol{p} + \Delta \boldsymbol{p} \boldsymbol{p}_J) \boldsymbol{I} \Big) + \xi_3 \boldsymbol{E}_\infty : (\boldsymbol{p}_J \boldsymbol{p}_J (\boldsymbol{p}_J \Delta \boldsymbol{p} + \Delta \boldsymbol{p} \boldsymbol{p}_J) + (\boldsymbol{p}_J \Delta \boldsymbol{p} + \Delta \boldsymbol{p} \boldsymbol{p}_J) \boldsymbol{p}_J \boldsymbol{p}_J - \frac{1}{3} (\boldsymbol{p}_J \Delta \boldsymbol{p} + \Delta \boldsymbol{p} \boldsymbol{p}_J) \boldsymbol{I} \Big). \quad (2.26)$$

The rate of change of $\Delta \boldsymbol{p}$ is computed from its evolution equation given by

$$\frac{d \Delta \boldsymbol{p}}{dt} = \boldsymbol{\omega}_{\mathrm{HI}} \times \boldsymbol{p}_J + \Delta \boldsymbol{p} \cdot \boldsymbol{R}_\infty + \lambda (\boldsymbol{E}_\infty \cdot \Delta \boldsymbol{p} - \boldsymbol{E}_\infty : (\Delta \boldsymbol{p} \boldsymbol{p}_J \boldsymbol{p}_J + \boldsymbol{p}_J \Delta \boldsymbol{p} \boldsymbol{p}_J + \boldsymbol{p}_J \boldsymbol{p}_J \Delta \boldsymbol{p})), \quad (2.27)$$

where $\boldsymbol{\omega}_{\mathrm{HI}}$ is the angular velocity obtained by evaluating a torque-free condition using the particle orientation $\boldsymbol{p}_J$ due to the velocity disturbance produced by the passing second ring. The first term is rotation driven by the gradient in the velocity disturbance produced by a suspension of noninteracting rings in the form of $\boldsymbol{\omega}_{\mathrm{HI}}$. The second and third terms together are the rotation rates relative to Jeffery rotation driven by the shear flow acting on the perturbation of $\boldsymbol{p}$ relative to $\boldsymbol{p}_J$. For a given set of initial conditions, the value of $d\Delta \boldsymbol{p}/dt$ for the renormalized equation matches the original calculation at $O(\Delta r^{-3})$. Thereby the value of

$\boldsymbol{p}_J + \Delta\boldsymbol{p}$ from the linearized equation also matches $\boldsymbol{p}$ from the original calculation at $O(\Delta r^{-3})$. The linearized equation for the stresslet (2.26) also matches $\boldsymbol{S}_{Hyd}(\boldsymbol{p}) - \boldsymbol{S}_{Hyd}(\boldsymbol{p}_J)$ of the original calculation at $O(|\Delta\boldsymbol{p}|) = O(\Delta r^{-3})$. Thus, subtracting the time integral of $\Delta\boldsymbol{S}^{RN}_{Hyd}$ from the time integral in Eq. (2.22) gives a convergent summation. The ensemble average $\Delta\boldsymbol{S}^{RN}_{Hyd}$ for the renormalization procedure is given by

$$\frac{\left\langle \boldsymbol{S}^{RN}_{p} \right\rangle}{n} = 0 = \sum_j \frac{A_j}{N_j} \sum_{k=1}^{N_j} (\Delta\boldsymbol{r}_0)_k \cdot \hat{\boldsymbol{\Gamma}}_\infty \left[\int_{-\infty}^{t_{HI}} dt\ \Delta\boldsymbol{S}^{RN}_{Hyd}(\Delta\boldsymbol{p}_i, \boldsymbol{p}_J(t, C_i, \tau_i)) + \int_{t_{HI}}^{\infty} dt\ \Delta\boldsymbol{S}^{RN}_{Hyd}(\Delta\boldsymbol{p}_f, \boldsymbol{p}_J(t, C_f, \tau_f)) \right], \tag{2.28}$$

where the subscripts i, f in the orbit constant, C, the phase angle τ, and $\Delta\boldsymbol{p}$ refer to the values at the beginning ($t \to -\infty$) and end ($t \to +\infty$) of the particle trajectory in the original calculation. Choosing the same values of initial and final orbit constants, phase angles, and the relative initial separation in the $\hat{\boldsymbol{\Omega}}_\infty\hat{\boldsymbol{\Gamma}}_\infty$ plane allows us to use the renormalization process for each individual trajectory and, thus, reduce the statistical error in the Monte-Carlo summation. Furthermore, the calculation from $t \in (-\infty, t_{HI})$ is termed as the forward-RN-trajectory and from $t \in (t_{HI}, \infty)$ is termed as the reverse-RN-trajectory. For the reverse RN-trajectory, the integration is performed in the reverse time direction and the starting particle separation in the flow-direction equal to the final value of $\Delta\boldsymbol{r} \cdot \hat{\boldsymbol{U}}_\infty$ at the end of the original calculation. When the original trajectory of particle I relative to particle II crosses the flow-vorticity plane, the initial flow-position for the reverse-RN-trajectory is chosen to be positive. This choice would be a reverse-RN-trajectory that is equivalent to the particle II starting at a position $(-\Delta\boldsymbol{r}_0 \cdot \hat{\boldsymbol{U}}_\infty, \Delta\boldsymbol{r}_0 \cdot \hat{\boldsymbol{\Omega}}_\infty, -\Delta\boldsymbol{r}_0 \cdot \hat{\boldsymbol{\Gamma}}_\infty)$ with same initial orientations.

The renormalized ensemble average of $\boldsymbol{S}_p$ is calculated from the following equation:

$$\frac{\langle \boldsymbol{S}_p \rangle}{n} = \sum_j \frac{\langle \boldsymbol{S}_p \rangle_j}{n} = \sum_j \frac{A_j}{N_j} \sum_{k=1}^{N_j} (\Delta\boldsymbol{r}_0)_k \cdot \hat{\boldsymbol{\Gamma}}_\infty \left\{ \int_{-\infty}^{\infty} dt[\boldsymbol{S}_{Hyd}(\boldsymbol{p}) - \boldsymbol{S}_{Hyd}(\boldsymbol{p}_J(t, \tau_i, C_i))(1 - H(t - t_{HI})) - \boldsymbol{S}_{Hyd}(\boldsymbol{p}_J(t, \tau_f, C_f))H(t - t_{HI})] - \int_{-\infty}^{t_{HI}} dt\ \Delta\boldsymbol{S}^{RN}_{Hyd}(\Delta\boldsymbol{p}, \boldsymbol{p}_J(t, C_i, \tau_i)) - \int_{t_{HI}}^{\infty} dt\ \Delta\boldsymbol{S}^{RN}_{Hyd}(\Delta\boldsymbol{p}, \boldsymbol{p}_J(t, C_f, \tau_f)) \right\}. \tag{2.29}$$

The convergence of the viscosity correction term $\langle S_p \rangle$ using this renormalization is given in Fig. 2(c). The value of $\langle S_p \rangle$, similar to $\langle S_f \rangle$, also does not change much as the domain size is increased from $(L_2, L_3) = (1.9, 1.9)$ to $(L_2, L_3) = (7.6, 7.6)$. The same renormalization strategy was also used for obtaining the moments of $\boldsymbol{p}$ in Eq. (2.16),

$$\frac{\langle \boldsymbol{pp} \rangle}{n} = \sum_j \frac{A_j}{N_j} \sum_{k=1}^{N_j} (\Delta\boldsymbol{r}_0)_k . \hat{\boldsymbol{\Gamma}}_\infty \left\{ \int_{-\infty}^{\infty} dt[\boldsymbol{p}(t)\boldsymbol{p}(t) - \boldsymbol{p}_J(t, \tau_i, C_i)\boldsymbol{p}_J(t, \tau_i, C_i)(1 - H(t - t_{HI})) - \boldsymbol{p}_J(t, \tau_f, C_f)\boldsymbol{p}_J(t, \tau_f, C_f)H(t - t_{HI})] - \int_{-\infty}^{t_{HI}} dt\ (\Delta\boldsymbol{p}\boldsymbol{p}_J + \boldsymbol{p}_J\Delta\boldsymbol{p}) - \int_{t_{HI}}^{\infty} (\Delta\boldsymbol{p}\boldsymbol{p}_J + \boldsymbol{p}_J\Delta\boldsymbol{p}) \right\}. \tag{2.30}$$

A list of various contributions to the particle stress through the stresslet tensors discussed here is mentioned in Table III. The contributions to the stresslet tensor averaged over all trajectories, i.e, $\langle \boldsymbol{S}_{con} \rangle$, $\langle \boldsymbol{S}_p \rangle$, and $\langle \boldsymbol{S}_f \rangle$, are all proportional to the non-dimensional number density n. $\langle \boldsymbol{S}_p \rangle$ and $\langle \boldsymbol{S}_f \rangle$ need a renormalization procedure for numerically calculating their values. The relative increase in the suspension viscosity and the normal stress-differences are defined in Secs. III D and III E, respectively.

D. Procedure for computing the steady state orbit distribution

The orientation distribution of rings in a dilute suspension is described by an orbit distribution and a phase angle with a uniform distribution from $[0, 2\pi)$. The procedure used to obtain this steady state orbit distribution is described here. We start with a set S_C of N_{set} orbit constant values, C, where C is assigned according to an arbitrarily chosen orbit distribution. Two values of C are randomly chosen from S_C and assigned to the two particles in the PI simulation. The value

of C for each particle is replaced by the new C value attained by the corresponding particle at the end of the interaction. This process is continued until the moments of orientation reach a statistical steady state value as a function of the number of such PI trajectories, N_{PI}. The initial separation in the gradient direction, Δr_3, was chosen between $(0,\ L_3]$ with a probability of $2\Delta r_3/L_3^2$, proportional to the flux of particles, and Δr_2 was chosen with a uniform probability between $[-L_2, L_2]$ as shown in Fig. 3(a). The strongest interactions determining the steady state orientation distribution involve particle separations of $O(1)$ similar to what has been observed for fiber suspensions [24]. The steady state orientation distribution was first obtained for $L_2 = 2$ and $L_3 = 1$, which corresponds to the ideal solid-body collision cross section of a tumbling and an aligned ring, which is described later in Sec. III B. This orbit distribution is used to start a simulation with a larger value of L_2 and L_3 until a new steady state orbit distribution is attained for the larger domain size. This process of increasing the domain size and using the previous steady state orbit distribution to obtain a new orbit distribution is continued until the difference between the new and the initial orbit distribution for a given value of (L_2, L_3) becomes statistically insignificant. Our simulations suggest that $(L_2, L_3) = (3, 3)$ provided nearly the same orientation distribution as a rectangular region with $L_2 = 2$, $L_3 = 1$ for the aspect ratios studied here. However, the number of simulated pairwise interactions required to reach steady state increased from $O(10^4)$ for the $(L_2, L_3) = (2, 1)$ rectangle to $O(10^5)$ for $(L_2, L_3) = (3, 3)$ rectangle since the number of simulations is proportional to Δr_3. Thus, the above systematic approach of obtaining a steady state orbit distribution by increasing the domain size is computationally efficient. This estimate can also be systematically improved by increasing the number of elements of the set S_C describing the orientation distribution.

The initial values of C in the set S_C were chosen from the probability distribution resulting from Jeffery rotation and weak anisotropic rotary diffusion, which is known to describe the orbit distribution of fibers in a dilute suspension [44,24]. The probability distribution of the modified orbit constant $C_b = C/(C + 1)$ with anisotropic diffusivity components is given by

$$p(C_b) = \frac{4C_b\phi_T^2\zeta}{\left(4\left(\frac{C_b}{1-C_b}\right)^2\phi_T^2\,\zeta\ +1\right)^{3/2}(1-C_b)^3}, \qquad (2.31)$$

where ζ is ratio of $\theta\theta$ and $\phi\phi$ diffusivity components [24]. The distribution in (2.31) with $\zeta = 1$ is also the *Leal-and-Hinch* distribution [30] for weakly Brownian disks, and this distribution was chosen to initialize the orientations in the set S_C as the base case. Additional simulations with $\zeta > 1$ were carried out to ensure that the same steady state distribution was obtained irrespective of the initial starting distribution. Furthermore, Eq. (2.31) was found to be a good approximation for the final steady state orbit distribution $p_{sim}(C_b)$ after using a suitable value of ζ. The values of ζ that best fit the simulation data are mentioned in Table IV. Figures 3(b) and 3(c) show the probability distribution from the simulation $p_{sim}(C_b)$ (symbols) and the fit using Eq. (2.27) with $\zeta = 1.43$ for $\bar{A} = 40$ rings and $\zeta = 0.50$ for $\bar{A} = 10$ rings, respectively. The orbit distributions set by PIs has a modest difference from the Leal and Hinch orbit distribution shown by the dashed line in Figs. 3(b) and 3(c). The best fit value of ζ for the steady orbit distribution obtained from PI simulations is shown in Table IV. These values of ζ were $O(1)$ for the aspect ratios studied here and appear to increase slowly with the aspect ratio.

The average and standard deviation of the moments of $\boldsymbol{p}$ from each region are obtained by binning the data until the standard deviation of the moments is converged. The duration of the simulation is quantified by $\tilde{N}_{sim} = N_{sim}/B$, where B is the number of elements in the bin, N_{sim} is the total number of pairwise interactions. The value of $\langle\cos^2(\theta)\rangle_J$ with 95% confidence limits was found to be $\{0.0905 \pm 0.0014,\ 0.0978 \pm 0.0015,\ 0.0933 \pm 0.0011\}$ for the regions defined by $(L_2, L_3) = \{(2, 1),\ (2, 2), (3, 3)\}$, respectively. Here, $\langle\rangle_J$ is an average value over steady state orbit distribution. The values of $\langle\cos^2(\theta)\rangle_J$ and $\langle\sin^2(2\phi)\sin^4(\theta)\rangle_J$ for different regions as functions of $\tilde{N}_{sim}$ are shown in Figs. 3(d) and 3(e), respectively. Figures 3(d) and 3(e) also show a case where the initial orbit distribution obtained from $\zeta = 3$ was used. This case rapidly converges to the steady state orbit distribution. We also performed simulations with initial orbit distributions that deviated significantly from the Leal and Hinch distribution, such as starting all particles in the $C = 0$ orbit (not shown in the figure), for smaller aspect ratio cases. The orbit distribution converged to the same steady state orbit distribution for all choices of initial distributions, within the statistical uncertainty of the numerical scheme. Starting further away from the initial condition required an algebraically larger number of simulations and, thus, a proportionally greater computational effort. The mean of the orientation moments obtained from the region defined by $(L_2, L_3) = (2, 2)$, which encompasses all particle collisions, was within $\pm 10\%$ of the corresponding means obtained from larger values of (L_2, L_3) for all aspect ratios studied here.

III. STRUCTURE AND RHEOLOGY OF DILUTE RING SUSPENSIONS

A. Position and orientation trajectories of particles

At dilute particle concentrations ($n \ll 1$), pairwise hydrodynamic interactions and particle contacts are important in determining the orientational dispersion, hydrodynamic diffusivity, and the particle stresses. The dependence of these quantities on the effective inverse-aspect ratio of the particle ϕ_T and the slenderness parameter $\epsilon = 1/\ln(8A)$ is also derived based on scaling arguments. The steady state orientation distribution moves $\boldsymbol{p}$ near the $C \to O(\phi_T^{-1})$ orbits as explained at the end of Sec. II D. Projections of trajectories of the relative position of the two particles in the flow-gradient and flow-vorticity planes are shown in Figs. 4(a) and 4(b) for contacting (−) and non-contacting (--) encounters. The initial cross-stream separations were similar for the

TABLE III. List of parameters determining the particle stress in the suspension.

Symbols	Description
$\boldsymbol{S}_{Hyd}$	Stresslet tensor of an isolated force-and-torque free ring in a simple-shear-flow with orientation $\boldsymbol{p}$
$\langle \boldsymbol{S}_{Hyd} \rangle_J$	Ensemble average stresslet exerted by isolated tumbling rings in an SSF
$\langle \boldsymbol{S}_p \rangle$	Ensemble average of the transient deviation of $\boldsymbol{S}_{Hyd}$ from $\langle \boldsymbol{S}_{Hyd} \rangle_J$ during all realizations of pairwise interactions
$\langle \boldsymbol{S}_{con} \rangle$	Ensemble average stresslet associated with all possible contact interactions
$\langle \boldsymbol{S}_{PI} \rangle$	Total stresslet contribution from pairwise interactions $=\langle \boldsymbol{S}_p \rangle + \langle \boldsymbol{S}_{con} \rangle + \langle \boldsymbol{S}_f \rangle$
$\Delta\mu$	Viscosity increase in suspension relative to the fluid viscosity
$\langle N_1 \rangle$	First normal stress-difference $\langle N_1 \rangle = n^2 \, (\langle \boldsymbol{S}_{PI} \rangle / n) : (\hat{\boldsymbol{U}}_\infty \hat{\boldsymbol{U}}_\infty - \hat{\boldsymbol{\Gamma}}_\infty \hat{\boldsymbol{\Gamma}}_\infty)$
$\langle N_2 \rangle$	Second normal stress-difference $\langle N_2 \rangle = n^2 \, (\langle \boldsymbol{S}_{PI} \rangle / n) : (\hat{\boldsymbol{\Gamma}}_\infty \hat{\boldsymbol{\Gamma}}_\infty - \hat{\boldsymbol{\Omega}}_\infty \hat{\boldsymbol{\Omega}}_\infty)$
$N_{i,1}$	Various contributions to the first normal stress difference from the different contributions of the stresslet tensor ($i = \{p, con, f\}$)
$N_{i,2}$	Various contributions to the second normal stress difference from the different contributions of the stresslet tensor ($i = \{p, con, f\}$)
$\boldsymbol{S}_f^{RN}$	The linearized part of $\boldsymbol{S}_f$ that averages to zero across all pairwise interactions, used for renormalized summation of $\boldsymbol{S}_f$
$\Delta\boldsymbol{S}_{Hyd}^{RN}$	The linearized part of $\boldsymbol{S}_p$ that averages to zero across all pairwise interactions used for renormalized summation of $\boldsymbol{S}_p$
$\boldsymbol{p}_J(C, \tau)$	Jeffery trajectory associated with the orbit constant C and phase angle τ
$\Delta\boldsymbol{p}$	Linearized change of the particle orientation relative to the Jeffery trajectory $\boldsymbol{p}_J$ used for renormalized calculation of $\boldsymbol{S}_p$

two types of encounters. The projections of the orientation of particle I, $\boldsymbol{p}_I$, along the flow and vorticity direction are shown in Figs. 4(c) and 4(d) along with the respective Jeffery trajectories using the phase angle and orbit constants for $\Delta r_1 \to \pm\infty$. A video illustrating these changes is also attached in the supplementary material [54] (non_contacting.avi, contacting.avi). Figures 4(a) and 4(b) illustrate that particle contact leads to a larger, $O(1)$, change in Δr_2 and Δr_3 at the end of the interaction compared to a corresponding smaller, $O(\epsilon)$, change from a trajectory involving purely hydrodynamic interactions. Additionally, a typical particle contact event lasts for an $O(1)$ time. In Figs. 4(c) and 4(d),

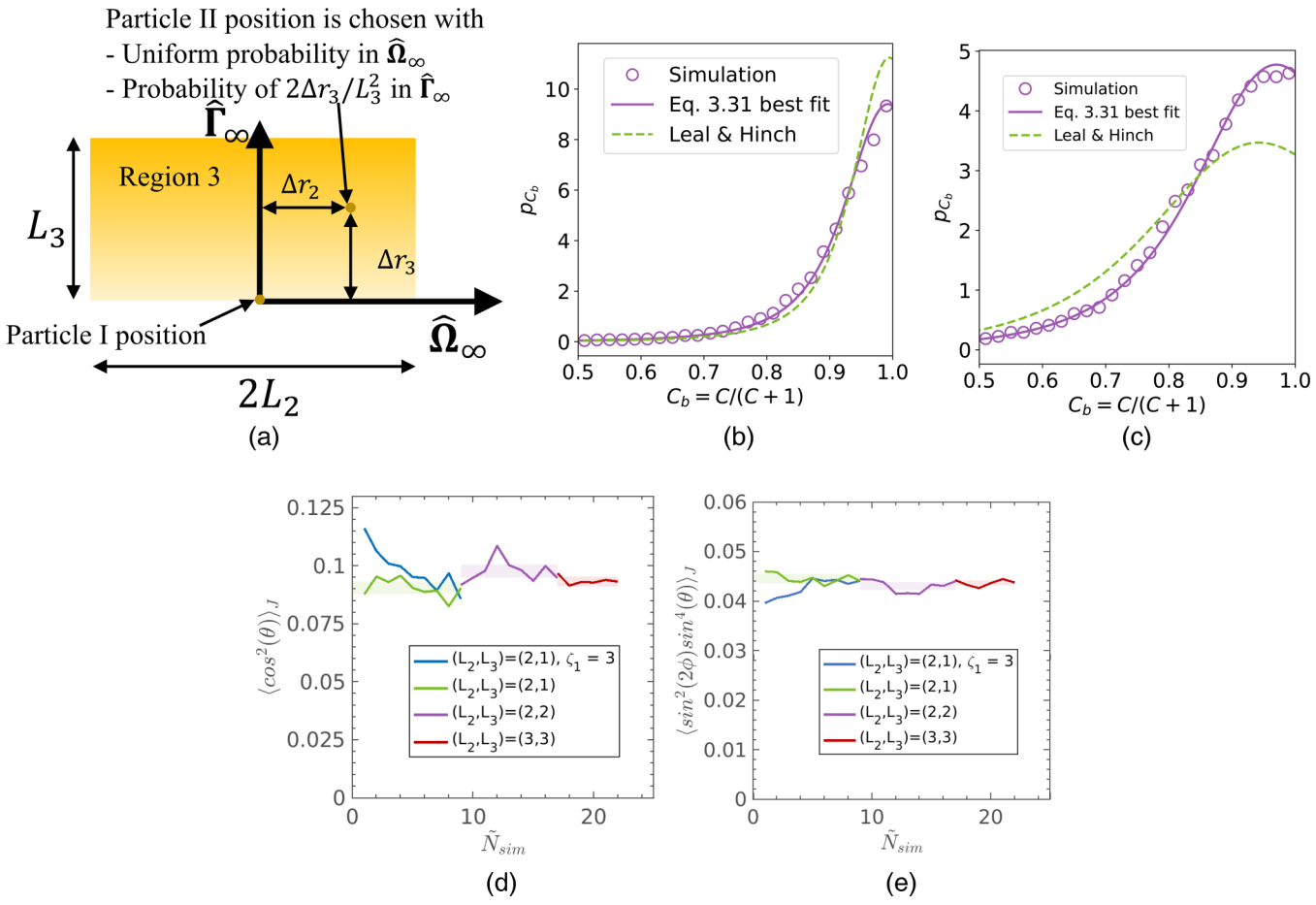

FIG. 3. (a) The kth region in the vorticity-gradient plane defined by (L_2, L_3) used for obtaining the steady-state orbit distribution. Probability of the modified orbit constant $C/(C+1)$ from simulation (symbols), $p(C_b)$ using Eq. (2.26) with ζ_1 from Table IV (solid line) and distribution of [30], i.e., $\zeta_1 = 1$, (dashed line) for (b) $\bar{A} = 40$ and (c) $\bar{A} = 10$. The values of (d) $\langle \cos^2(\theta) \rangle_J$ and (e) $\langle \sin^2(2\phi)\sin^4(\theta) \rangle_J$ as functions of $\tilde{N}_{sim}$ for an $\bar{A} = 40$ ring with different values of (L_2, L_3). The curves for regions $(L_2, L_3) = (2, 2)$ and $(3, 3)$ in (d) and (e) are shifted on the x-axis by 9 and 17 units, respectively, for visual purpose. The number of elements in the bins in the averaging process for the four legends in order is $B = \{10^3, 10^3, 2 \times 10^3, 2 \times 10^4\}$.

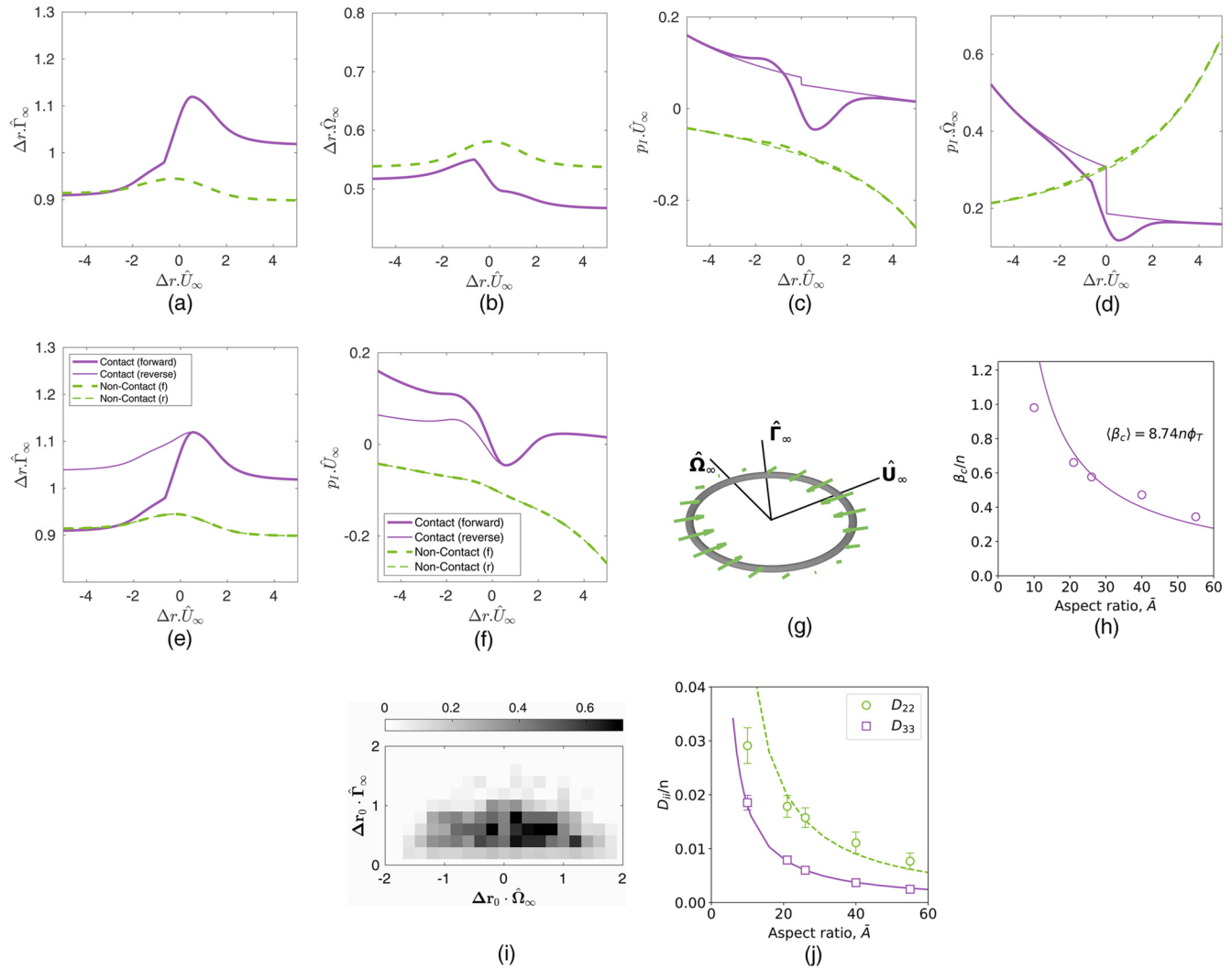

FIG. 4. The projections of trajectories of relative positions of the center of mass of the two rings in the (a) flow-gradient and (b) flow-vorticity planes for an aspect ratio $\bar{A} = 21$ particle. Projection of $\boldsymbol{p}_I$ in the (c) flow ($\sin(\phi)\sin(\theta)$) and (d) vorticity ($\cos(\theta)$) directions, where thin lines represent Jeffery trajectories using the phase angle and orbit constants at $\Delta r_1 \to \pm\infty$. Solid line (−) is a particle trajectory involving mechanical contact and dashed line (--) is a trajectory with purely hydrodynamic interaction. The initial separation of the particles making mechanical contact is ($\Delta r_2 = 0.52$, $\Delta r_3 = 0.91$) and those having purely hydrodynamic interactions is ($\Delta r_2 = 0.54$, $\Delta r_3 = 0.91$). The contacting event occurs between $-0.70 \le \Delta r_1 \le 0.56$ (Videos of these trajectories are in the supplementary material [54]). (e) Relative position of particles in the flow-gradient plane and (f) projection of $\boldsymbol{p}_I$ in the flow direction for the flow-reversed trajectory (thin lines) of the original (forward) particle trajectories shown in figure (a)–(d), for contacting (- solid) and non-contacting (--) scenarios. (g) Force-distribution for an $\bar{A} = 21$ ring in the $C \to \infty$ orbit that has $|\boldsymbol{f}_{SSF}| \propto \sin(2\phi)$. (h) Collision frequency of particles as a function of $\bar{A}$ along with the scaling fit. (i) Probability density function of particle contact in the vorticity-gradient plane for an $\bar{A} = 21$ ring. (j) Translational diffusivity in the vorticity (D_{22}) and gradient (D_{33}) directions as a function of the aspect ratio $\bar{A}$. The scaling fits using Eq. (3.2) are also shown.

it is also visually apparent that deviation of $\boldsymbol{p}$ from the Jeffery trajectory is larger for contacting trajectories compared to the non-contacting ones. Particle contact prevents the free tumbling of particles and the two particles tend to rotate as a pair as shown in the animation. These trajectories showcase the importance of incorporating effects of particle contact in addition to hydrodynamic interaction when studying the motion of particles in a dilute ring suspension.

Upon the reversal of the shear flow, the position and orientation of the two rings should return to their initial values if the interactions are purely hydrodynamic in nature due to Stokes flow reversibility. This is confirmed in our simulations as shown in Fig. 4(e), wherein the original (forward) trajectory (-- thick) and the flow-reversed (-- thin) trajectory overlap. Trajectories that include particle contact break the flow-reversal symmetry because contact force is non-zero when the particles approach each other and is zero when they move apart [40]. This is evident from the difference in forward (- thick) and reverse (- thin) trajectories as shown in Fig. 4(e). The particle orientation also breaks the flow-reversal symmetry for contacting trajectories as shown in Fig. 4(f).

TABLE IV. The best fit values of ζ obtained by matching the $p_{sim}(C_b)$ to the orbit distribution set by Eq. (2.31).

$\bar{A}$	ζ
10	0.50
21	0.92
26	1.27
40	1.43
55	1.44

Figure 4(g) shows the force distribution $\boldsymbol{f}_{SSF}$ of an $\bar{A} = 21$ ring tumbling in the $C \to \infty$ orbit. The components of this force are given by $f_{SSF,n} = \gamma_1 \, (f_{n1}/\gamma_1 \cos(s) + f_{n3}/\gamma_1 \cos(3s))$, $f_{SSF,b} = \gamma_1 (f_{b4}/\gamma_1 \sin(s) + f_{n3}/\gamma_1 \sin(3s))$, and $f_{SSF,p} = 0$, where $\gamma_1 = \boldsymbol{nn}:\hat{\boldsymbol{U}}_\infty \hat{\boldsymbol{\Gamma}}_\infty = 0.5 \sin(2\phi)$ and $0 \le s < 2\pi$ is the position along the ring centerline, s being zero at $\boldsymbol{r}_c = (1 - \bar{A}^{-1})\boldsymbol{n}$. The parameters f_{n1}/γ_1, f_{n3}/γ_1, and f_{b4}/γ_1 are independent of the orientation, and their values as functions of $\bar{A}$ are shown in Fig. 9(c). The velocity disturbance pulls fluid inward in the plane of the ring when $\sin(2\phi) < 0$ and pushes it outward along $\pm\boldsymbol{p}$. This fluid velocity distribution is analogous to that caused by an equivalent fiber with a 90° rotation in ϕ.

B. Collision frequency and translational hydrodynamic diffusivity

The rate of particle collisions is obtained from the flux of particles that collide with each other. The collision frequency of rings β_c is, thus, given by

$$\frac{\beta_c}{n} = \sum_j \frac{A_j}{N_j} \sum_{k=1}^{N_j} (\Delta \boldsymbol{r}_0)_k \cdot \hat{\boldsymbol{\Gamma}}_\infty |_{|\boldsymbol{F}_{con}|>0}, \tag{3.1}$$

where the inner summation is non-zero only when mechanical contact occurs between the two particles. In all our simulations, contact is assumed when the minimum separation of the particles is $10^{-2}A^{-1}$. As discussed earlier, the largest contributors to the collision frequency are tumbling-aligned interactions, and therefore, β_c scales as ϕ_T. Figure 4(h) shows the variation of β_c with the aspect ratio $\bar{A}$ and its dependence is approximately given by $8.74 n\phi_T$. This scaling is similar to the ideal collision frequency of disks whose value equals $13.12\, n\phi_T$, with ϕ_T being the effective-inverse-aspect ratio of the disk [17]. The ideal collision frequency for disks is higher because that calculation neglects long-range hydrodynamic interaction, and the central hole of the ring also reduces the possible area in the phase space available for collision. The rate of collision per unit volume is given by $0.5 n\beta_c = 4.37\, n^2\phi_T$ in a dilute suspension of slender rings. This collision frequency should give a representative measure of the contact stresses in the suspension that is discussed in Sec. III D. Particle contact frequency provides a measure of the degree of particle agglomeration in the suspension which can further impact the rheological properties in the presence of adhesive forces between the particles.

Figure 4(i) shows the probability density function of contacting events based on the relative initial separation of particles in the gradient-vorticity plane for an $\bar{A} = 21$ ring. The probability peaks near $\Delta r_3 = 0.8 = O(1)$ and $\Delta r_2 = 0$ and rapidly decays as the relative position approaches the boundary of the ideal collision cross section. The peak occurs at Δr_3 close to 1 because most collisions are between a flipping and aligned ring rather than two flipping rings ($\Delta r_3 = 2$) or two aligned rings ($\Delta r_3 = O(\bar{A}^{-1})$). The probability density has a steeper slope in the gradient direction than the vorticity direction, which is caused by the pinching of Jeffery orbits and the shape of the collision cross section of a tumbling and an aligned ring (which is a rectangle bound by $\Delta r_2 = \pm 2$, $\Delta r_3 = 0$ and $\Delta r_3 = 1$). This shape of the collision cross section was also the reason to choose $(L_2, L_3) = (2, 1)$ for obtaining the steady state orbit distribution earlier in Sec. II D. This qualitative shape of the density of contacting trajectories is similar for other high-aspect ratio rings.

Although each particle contact event generates a large change in the orientation and cross-stream position of the particles compared to non-contacting trajectories, the contacting events were observed to occur less frequently than the most important hydrodynamic interactions between a tumbling and an aligned ring. The contribution to stresses, orientational structure, and the translational diffusivities were found to have numerically comparable contributions from contacting and non-contacting trajectories as shown in the results hereafter.

The center of mass of a tumbling torus is displaced from its original fluid streamline due to particle contact and hydrodynamic interactions with other particles. The displacements are stochastic and the overall translation of the particle in the suspension appears to be diffusive in nature. This motion can be quantified using the hydrodynamic diffusivity and its components in gradient (D_{33}) and vorticity (D_{22}) directions are shown in Fig. 4(j). Particle contact between an aligned and tumbling ring leads to an $O(1)$ displacement of the ring in the gradient or vorticity direction, and this event has an $O(\phi_T)$ frequency. Contributions from purely hydrodynamic interactions toward diffusivity are $O(\epsilon^2\phi_T)$, but these long-ranged contributions to the diffusivity come from trajectories whose initial conditions extend well beyond the collision cross section. The contributions from particle contact and HI to the diffusivity were found to be numerically comparable at the aspect ratios studied here. For an aspect ratio 21 particle, the contributions to D_{33} from contacting and non-contacting trajectories are nearly equal, but the contacting trajectories only contribute to 15% of the total value of D_{22}. Similar proportions were observed at other aspect ratios studied here. The contributions from HIs and particle contact are added together using the above scaling argument to provide an empirical fit to the data given by

$$\frac{D_{22}}{n} = \frac{\bar{D}_{22}}{\gamma R^2 n^* R^3} = 3.17 \times 10^{-2}\phi_T + 5.60\epsilon^2\phi_T, \tag{3.2a}$$

$$\frac{D_{33}}{n} = \frac{\bar{D}_{33}}{\gamma R^2 n^* R^3} = 4.16 \times 10^{-2}\ \phi_T + 1.39\ \epsilon^2\phi_T, \tag{3.2b}$$

where $\bar{D}_{22}$ and $\bar{D}_{33}$ are the dimensional translational diffusion coefficients in the vorticity and gradient direction, respectively. Extending the above formulae beyond the aspect ratio range studied here suggests that the second term becomes negligible only for $\bar{A} \gg O(10^4)$, which are aspect ratios of little practical importance. Thus, for most practical aspect ratios, the contributions of both contacting and non-contacting trajectories are expected to be important, and this feature is observed for other results presented hereafter.

The values of D_{22} deviate from the fit given by Eq. (3.2a) for $\bar{A} = 10$ rings. The scaling arguments derived for D_{22} and other particle properties only consider the fact that $\langle C \rangle_J = O(\phi_T^{-1})$ and $\sqrt{\langle \phi^2 \rangle_J} = O(\phi_T)$, implicitly obtained from the Leal and Hinch (LH) distribution given by Eq. (2.31) with $\zeta = 1$, and ignores any weaker dependence of the orientation structure on $\bar{A}$ arising from changes of the orbit distribution. $\bar{A} = 10$ rings are closer to the $C \to \infty$ orbit than rings with LH distribution as shown in Fig. 3(c), and thus, the magnitude of $\boldsymbol{f}_{SSF}$ during a tumbling event should be numerically smaller than the one expected from LH distribution. The deviation from the scaling result was strongest for non-contacting trajectories, which could be explained from the reduced strength of $\boldsymbol{f}_{SSF}$. The deviation in the simulation values from scaling was also more prominent for D_{22}, which has a dominant contribution from pure HIs. This deviation in the simulation values from the scaling fits was also observed for other particle properties for $\bar{A} = 10$ rings as discussed later.

The translational diffusivity in the gradient direction for fibers is given by $\bar{D}_{33} = \gamma \bar{n} l^5 1.1 \times 10^{-2}\, \bar{A}^{-1} \ln^{-2}(2\bar{A})$ [41]. The numerical value is orders of magnitude smaller than the corresponding value for rings computed from Eq. (3.2b) in the aspect ratio range $\bar{A} = 10 - 55$. The numerical value of D_{33} for aspect ratio 21 rings is $7.89 \times 10^{-3} n$, which is two orders of magnitude larger than the value of $D_{33} = 3.8 \times 10^{-5} n$ in an equivalent fiber suspension. Similar proportions are expected for D_{22} as well. The curved-centerlines of the cross section of two rings in a shear flow will on an average approach to within shorter distances than two equivalent fibers (which are rotating line-segments), a purely geometric effect. Thus, purely hydrodynamic interactions are also expected to be stronger in rings than in fibers. Additionally, rings have a significant cross-streamline displacement from interparticle contact. The hydrodynamic diffusivity in a dilute disk suspension, which has not been reported yet, should also be driven by particle contact and $O(1)$ fluid velocity disturbances and, thus, scale as ϕ_T at high aspect ratios.

C. Orientational structure of ring suspensions

To quantify the extent to which planar particles such as rings align so that the plane of the particle lies in flow-vorticity plane, we define a flow alignment parameter k as the ensemble average value of $1.5(1 - p_3^2)$. The value of k is unity for an isotropic distribution and equal to zero for perfect particle alignment in the flow-vorticity plane. This parameter determines the orientational order in the suspension, which is important for quantifying the anisotropy of the microstructure of materials processed from such suspensions. In the dilute limit, the flow-alignment parameter can be written as $k = k_0 + k_1 n + O(n^2)$, where $k_0 = 1.5\langle 1 - p_{3,J}^2 \rangle_J$, with $\langle \rangle_J$ being an average over the steady state orbit distribution and Jeffery rotation period; and $k_1 n = 1.5\langle p_3^2 - p_{3,J}^2 \rangle$, with $\langle \rangle$ being an ensemble average over all possible realizations of PIs. The values of k_0 and k_1 as functions of $\bar{A}$ are shown in Figs. 5(a) and 5(b), respectively. k_0 provides the average tilt of isolated rings in Jeffery rotation due to the steady state orbit distribution and is, thus, proportional to ϕ_T, the best fit being $k_0 = 3.24\phi_T$. In this scaling, the assumption is that the orbit distribution is purely a function of the effective inverse-aspect ratio ϕ_T and has no other dependence on the aspect ratio $\bar{A}$. This assumption works well for $\bar{A} \geq 21$ but breaks down for $\bar{A} = 10$ rings. This causes most scaling laws described in this work to deviate from simulation results for $\bar{A} = 10$ rings. The positive value of k_1 shown in Fig. 5(b) suggests that PIs decrease the flow alignment relative to isolated particles. This reduction in flow alignment during PIs is caused by a greater dispersion in the ϕ and θ direction. The value of $\langle \sin^2(\phi) \rangle - \langle \sin^2(\phi) \rangle_J$ provides a measure of dispersion of $\boldsymbol{p}$ along the ϕ direction, while $\langle \cos^2(\theta) \rangle - \langle \cos^2(\theta) \rangle_J$ is used as a measure of dispersion of $\boldsymbol{p}$ along the θ direction.

Figure 5(c) shows the value of $\left(\langle \sin^2(\phi) \rangle - \langle \sin^2(\phi) \rangle_J\right)/n$ as a function of $\bar{A}$ where $\langle \sin^2(\phi) \rangle_J = \phi_T/(1 + \phi_T)$ is the value corresponding to an isolated tumbling ring based on Jeffery rotation. The positive value of $\langle \sin^2(\phi) \rangle - \langle \sin^2(\phi) \rangle_J$ implies that the typical value of ϕ subtended by interacting rings is greater than an isolated tumbling ring. An aligned ring blocks the rotation of a tumbling ring when the particles make contact, leading to an $O(1)$ value of ϕ for an $O(1)$ contacting time. This explains the positive sign of $\langle \sin^2(\phi) \rangle - \langle \sin^2(\phi) \rangle_J$ and its proportionality with the $O(\phi_T)$ collision frequency discussed in Sec. III B. Purely hydrodynamic interactions also increase the dispersion in the ϕ-direction, which was also observed in fiber suspensions at concentrations $n < \bar{A}$ [28]. The contributions from contacting and non-contacting trajectories to $\langle \sin^2(\phi) \rangle - \langle \sin^2(\phi) \rangle_J$ were found to be comparable in magnitude. The value $1.57\phi_T$ fit the simulation data in Fig. 5(c) well. The change in tumbling rate relative to the Jeffery tumbling rate was quantified by evaluating Eq. (2.13) with the integrand equal to $\lim_{M \to \infty} \left(\frac{(\phi(M) - \phi(-M))}{2\pi} - \frac{2M}{T} - \frac{(\Delta\phi_{RN,f}(0) - \Delta\phi_{RN,r}(0))}{2\pi} \right)$, where $\Delta\phi_{RN} = (\Delta p_1 \cos(\phi_J) - \Delta p_3 \sin(\phi_J))/\sin(\theta_J)$ for respective renormalized trajectories. There was no change in the tumbling rate from Jeffery's tumbling rate within the statistical uncertainty of the calculation. Figure 5(d) shows the value of $\left(\langle \cos^2(\theta) \rangle - \langle \cos^2(\theta) \rangle_J\right)/n$ as a function of $\bar{A}$, which was positive for aspect ratios studied here. This suggests that the tilt of $\boldsymbol{p}$ from $\hat{\boldsymbol{\Gamma}}_\infty$ in the θ direction also increases on average during the interaction compared to the value based on Jeffery rotation in steady state orbit distribution.

A particle orientation also has a transient change in the modified orbit constant $C_b = C/(C + 1)$ during an interaction with another particle. The simulations suggest that the particles move away from the flipping orbit ($C_b \to 1$ or $C \to \infty$) during a typical interaction. This was quantified from the value of $n^{-1}\langle C_b - C_{b,J} \rangle$ as shown in Fig. 5(e) which is negative. This suggests that particles move away from the flipping orbit during the transient interaction, and this was found to be true on an average for both contacting and non-contacting trajectories. The shift away from the flipping orbit during a PI was also quantified through a transient average displacement in the

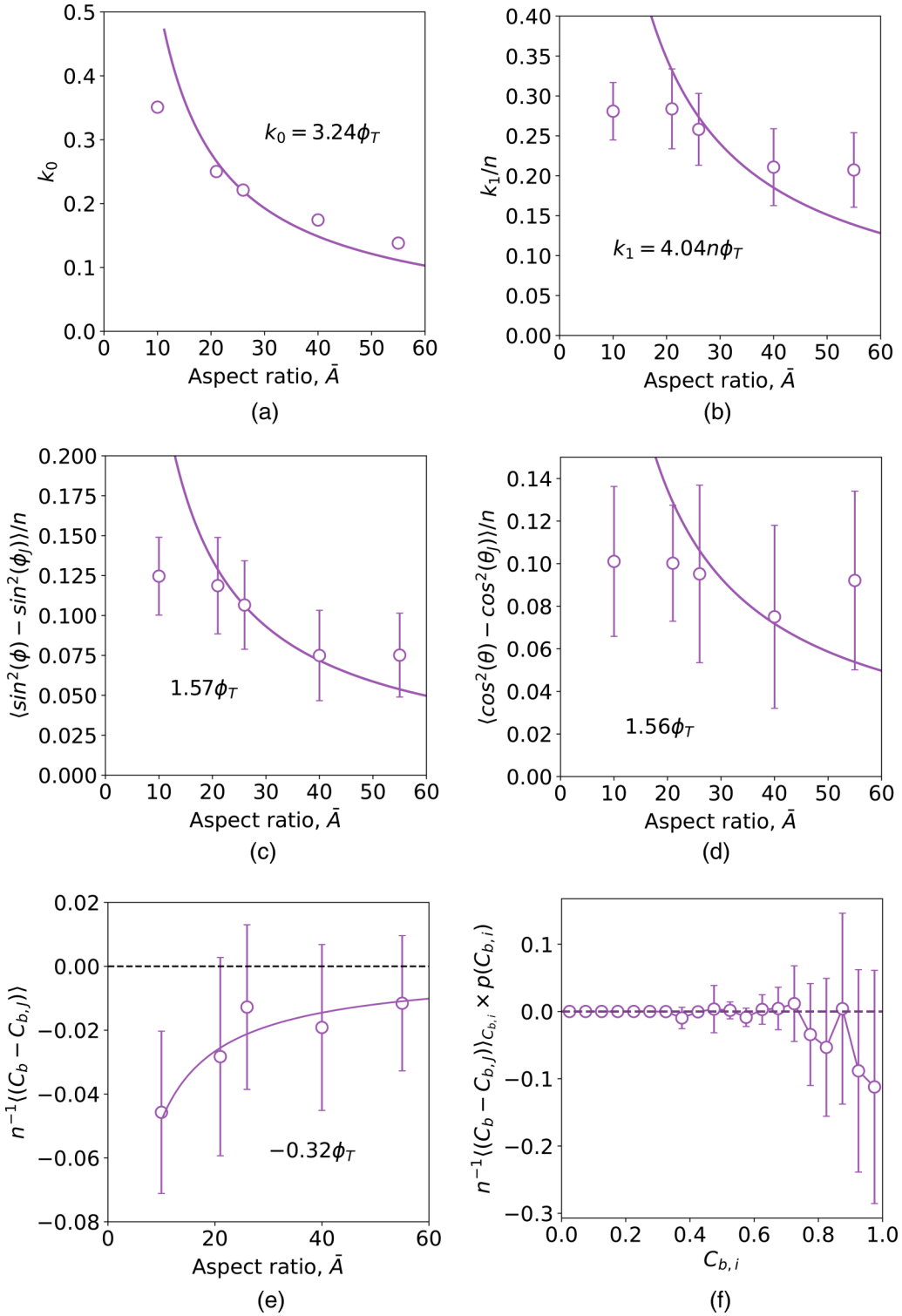

FIG. 5. Variation of (a) k_0, (b) k_1, (c) $\left(\langle \sin^2(\phi)\rangle - \langle \sin^2(\phi)\rangle_J\right)/n$, (d) $\left(\langle \cos^2(\theta)\rangle - \langle \cos^2(\theta)\rangle_J\right)/n$, and (e) $n^{-1}\langle C_b - C_{b,J}\rangle$ as a function of the aspect ratio $\bar{A}$ along with the scaling fit. (f) $n^{-1}\langle C_b - C_{b,J}\rangle_{C_{b,i}} \times p(C_b)$, the ensemble average displacement experienced by a $\bar{A} = 21$ ring tumbling initially in an orbit specified by $C_{b,i}$, as a function of the initial orbit constant $C_{b,i}$ (circle). All error bars correspond to 95% confidence intervals.

modified orbit constant experienced by the particle orientation tumbling initially in an orbit specified by $C_{b,i}$ and this displacement termed as $n^{-1}\langle C_b - C_{b,J}\rangle_{C_{b,i}}$. The value of $n^{-1}\langle C_b - C_{b,J}\rangle_{C_{b,i}}$ is computed using Eq. (2.13) with $\boldsymbol{X} = C_b(t)$ and using the summation only for interactions with $C_b \in [C_{b,i} - \Delta_1, C_{b,i} + \Delta_1]$. Figure 5(f) shows $n^{-1}\langle C_b - C_{b,J}\rangle_{C_{b,i}}$ scaled with the steady state orbit distribution, $p_{sim}(C_{b,i})$, as a function of $C_{b,i}$ for an $\bar{A} = 21$ ring ($\Delta_1 = 0.05$). The negative sign of $n^{-1}\langle C_b - C_{b,J}\rangle_{C_{b,i}}$ suggests that on an average the particle orientation moves to lower C_b orbits during a PI. This would indicate that with increasing concentration the probability distribution in ring suspensions should move further away from the flipping orbits compared to the distribution shown in Figs. 4(b) and 4(c). Overall, there is a

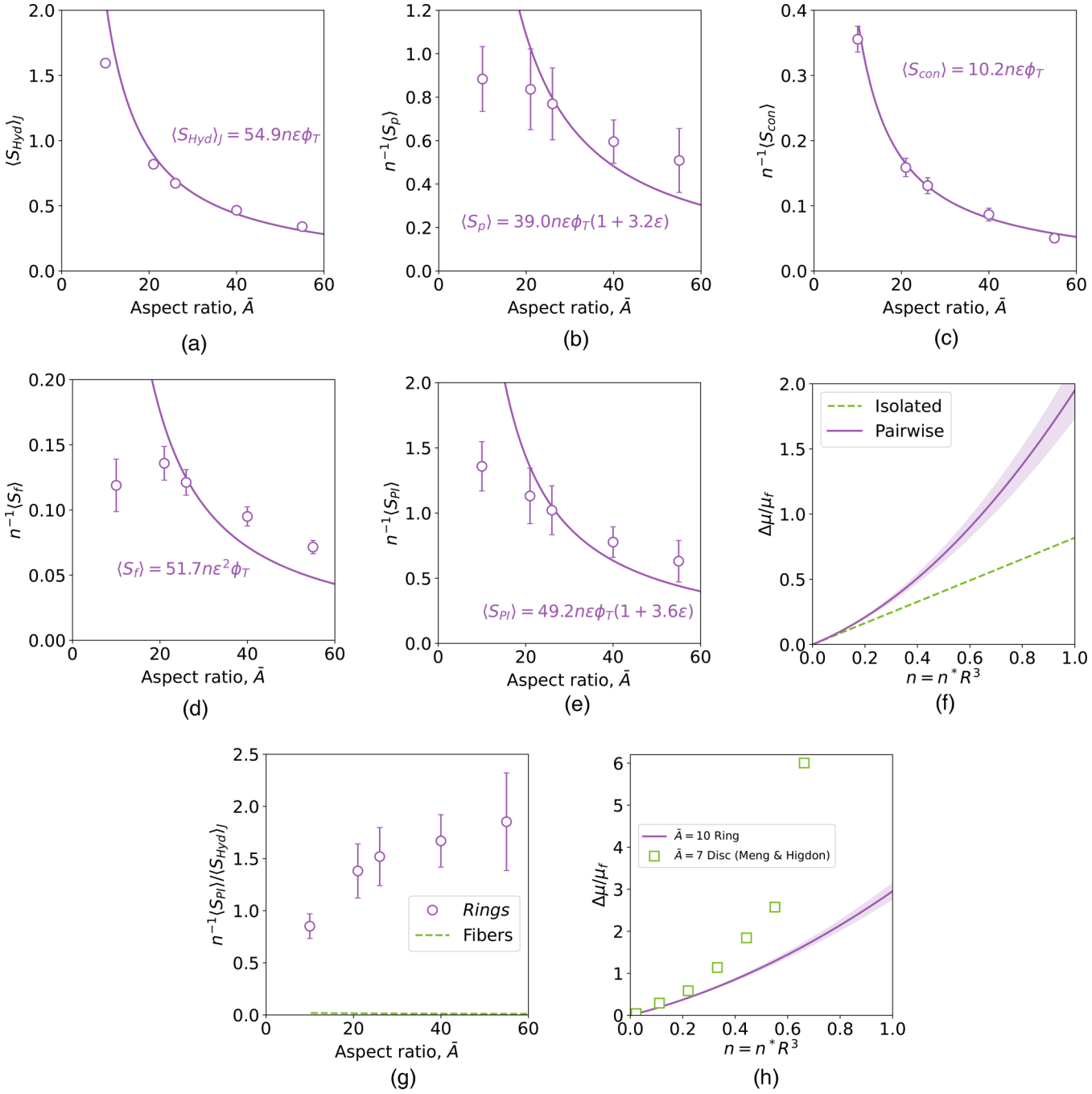

FIG. 6. (a) Leading order correction to the shear stress per particle or the (13) component of the stresslet tensor, $\langle S_{Hyd}\rangle$, obtained from the steady-state orbit distribution caused by PIs and $O(\epsilon\phi_T)$ scaling (line) discussed in the text. Components of $O(n^2)$ viscosity correction from (b) $\langle S_p\rangle$, (c) $\langle S_{con}\rangle$, and (d) $\langle S_f\rangle$; (e) $\langle S_{PI}\rangle$ as functions of $\bar{A}$ along with scaling fits. (f) $\Delta\mu/\mu_f$ as a function of n for $\bar{A} = 21$ rings using the isolated particle stresslet from (a) and the PI contribution obtained in (e). (g) The ratio, $\langle S_{PI}\rangle/(n\langle S_{Hyd}\rangle)$, of the coefficients of $O(n^2)$ and $O(n)$ terms in viscosity expansion as a function of the aspect ratio for rings (symbols) is compared with the value for fibers (dashed line) obtained from Eq. (3.6) using $C_m = 0.444$. (h) $\Delta\mu/\mu_f$ for $\bar{A} = 7$ disks formed by a planar collection of spheres in Meng and Higdon's simulations (symbols) and an $\bar{A} = 10$ ring (solid line). The error bars and the shaded regions represent 95% confidence intervals.

reduction in the flow-alignment during PIs and this increases the average stresses as discussed in Secs. III D–III F.

D. $O(n)$ and $O(n^2)$ correction to the shear viscosity

The rheology of a sheared suspension of rings can be described by a shear viscosity correction and normal stresses arising from particle contact. The correction to the suspension viscosity μ is given by

$$\frac{\Delta\mu}{\mu_f} = \frac{\mu-\mu_f}{\mu_f} = n\langle S_{Hyd}\rangle_J + n^2\left(\frac{\langle S_p\rangle}{n} + \frac{\langle S_f\rangle}{n} + \frac{\langle S_{con}\rangle}{n}\right), \tag{3.3}$$

where μ is the suspension viscosity and S_i, $i = \{Hyd, p,$

$f, con\}$, are the $\boldsymbol{S}_i{:}\hat{\boldsymbol{U}}_\infty\hat{\boldsymbol{\Gamma}}_\infty$ components of the corresponding stresslet tensors defined in Sec. II C. The coefficients of the $O(n^2)$ correction to the viscosity in Eq. (3.3) is termed $\langle S_{PI}\rangle n^{-1} = \left(\langle S_p\rangle + \langle S_f\rangle + \langle S_{con}\rangle\right)n^{-1}$. $\langle S_{Hyd}\rangle_J$ is the value of S_{Hyd} averaged over each Jeffery orbit and weighted with the steady state orbit distribution, $p_{sim}(C_b)$, described in Sec. II D. The value of $\langle S_{Hyd}\rangle_J$ is computed from the following equation:

$$\langle S_{Hyd}\rangle_J = \int_0^1 dC_b\, p_{sim}(C_b)\, \frac{1}{T}\int_0^T dt\, S_{Hyd}. \tag{3.4}$$

This simplifies to $\langle S_{Hyd}\rangle_J = 0.5(\xi_1+\xi_2) - 0.5\xi_2\langle\cos^2(\theta_J)\rangle_J + 0.25\xi_3\langle\sin^2(2\phi_J)\rangle\langle\sin^4(\theta_J)\rangle_J$. The first term $0.5(\xi_1+\xi_2) = O(\bar{A}^{-2})$ has a value that is numerically comparable to second and third terms of $O(\epsilon\phi_T\zeta^{0.5})$ at $\bar{A} = O(10)$. As shown in Fig. 6(a), $\langle S_{Hyd}\rangle_J$ (symbols) decreases with $\bar{A}$. The scaling $\langle S_{Hyd}\rangle_J = 54.88\epsilon\phi_T$ indicated by the line works well for $\bar{A} \geq 21$ but provides a poor estimate at $\bar{A} = 10$ for reasons described at the end of Sec. III B.

The value of $\langle S_p\rangle$ is driven by the change in $\boldsymbol{p}$ from its Jeffery trajectory, $\boldsymbol{p}_J$, during a PI. The variation in $n^{-1}\langle S_p\rangle$ with $\bar{A}$ is shown in Fig. 6(b). The contribution to $\langle S_p\rangle$ from contacting trajectories scales as $n\epsilon\phi_T$, which stems from an $O(1)$ change in $\boldsymbol{p}-\boldsymbol{p}_J$ during particle contacts that occurs with an $O(n\phi_T)$ frequency. Contributions from non-contacting trajectories lead to $O(\epsilon)$ changes in $\boldsymbol{p}-\boldsymbol{p}_J$ during the interaction of a tumbling and an aligned ring and, thus, contribute to $\langle S_p\rangle$ at $O(n\epsilon^2\phi_T)$. The simulations suggest that ensemble average contributions to $\langle S_p\rangle$ from contacting and non-contacting trajectories are numerically comparable to each other, although a typical contacting trajectory has a much larger contribution than a non-contacting trajectory. The positive value of $\langle S_p\rangle$ is also consistent with the results of Sec. III C wherein the flow-alignment was shown to reduce during PIs. An empirical expression $\langle S_p\rangle = 38.99\epsilon\phi_T n(1+3.16\epsilon)$ provides a good fit to the simulation data in the aspect ratio range of $21 \leq \bar{A} \leq 55$.

In addition to the aforementioned indirect contribution of particle contact, there is a more direct contribution to the suspension shear stress $n\langle S_{con}\rangle$ arising from the contact force. Particle contact induces a stress on the surface of the ring quantified through $\boldsymbol{f}_{con}$, which includes $\langle S_{con}\rangle$. The particles remain in contact for an $O(1)$ time and generate an $O(\epsilon)$ stresslet during a collision event. The variation in $\langle S_{con}\rangle$ with the aspect ratio is shown in Fig. 6(c) and is approximately given by $\langle S_{con}\rangle = 10.17\epsilon\phi_T n$ where the scaling is obtained by multiplying the $O(\phi_T)$ collision frequency with the $O(\epsilon)$ stresslet included in $\boldsymbol{f}_{con}$. This direct contribution to the stress, $\langle S_{con}\rangle$, is numerically comparable to the individual contributions from $\langle S_p\rangle$ and $\langle S_f\rangle$.

The final contribution to the $O(n^2)$ viscosity correction is $\langle S_f\rangle$, the direct effect of hydrodynamic interactions on the stresslet captured by the force distribution $\boldsymbol{f}_{HI}$. This contribution is shown in Fig. 6(d) and scales as $O(n\epsilon^2\phi_T)$ owing to $O(\epsilon)$ velocity disturbance generated by a tumbling ring near an aligned ring, the event itself occurring with an $O(n\phi_T)$ frequency. The tilt of a ring increases during a particle contact event compared to that in its Jeffery tumbling state, which is close to the tilt during non-contacting interactions as shown in Fig. 4. The larger tilt increases the magnitude of the velocity disturbance and the corresponding force per unit length $\boldsymbol{f}_{HI}$. The contact events also trigger an additional $O(\epsilon)$ force per unit length, $\boldsymbol{f}_{con}$, which affects the $O(\epsilon)$ velocity disturbance produced by the neighboring contacting ring. The simulations suggest that the contribution to $\langle S_f\rangle$ from contacting trajectories is around 65% compared to 35% contribution from non-contacting trajectories. A scaling fit of $\langle S_f\rangle = 51.68\epsilon^2\phi_T n$ matches the simulation results well for $21 \leq \bar{A} \leq 55$.

The net contribution to the stresslet from PIs, $\langle S_{PI}\rangle/n$, is shown in Fig. 6(e) and can be approximately fit by the scaling $\langle S_{PI}\rangle = 49.15n\epsilon\phi_T(1+3.56\epsilon)$. The value of $\langle S_{PI}\rangle$ decays as $O(n\epsilon\phi_T)$ for $\bar{A} > 21$, but the values flatten out at the smaller aspect ratio of $\bar{A} = 10$. This is caused by the differences in the sharpness of orbit distributions near $C_b \to 1$ between $\bar{A} = 10$ and the higher aspect ratio orbits as shown in Figs. 3(b) and 3(c). The variation in $\Delta\mu/\mu_f$ with n for an aspect ratio 21 particle is also shown in Fig. 6(f). Figure 6(f) indicates that the viscosity correction obtained by including PIs is twice the value for an isolated ring at $n = 1$. Overall, the value for the viscosity correction from two-ring interactions can be computed from Eq. (3.3) using the values presented in Figs. 6(a)–6(d). The scaling fit to approximate the correction to the suspension viscosity is given by

$$\frac{\Delta\mu}{\mu_f} = 54.88\epsilon\phi_T n(1+0.90(1+3.56\epsilon)n + O(n^2)). \tag{3.5}$$

Equation (3.5) provides a good approximation for $21 \leq \bar{A} \leq 55$.

The ratio $\langle S_{PI}\rangle/\left(n\langle S_{Hyd}\rangle\right)$, i.e., the ratio of the $O(n^2)$ and $O(n)$ coefficient in Eq. (3.3), for rings has a nearly constant value of $O(1)$ similar to that in a suspension of spheres [43]. For comparison, this ratio for dilute fiber suspensions has a much smaller value that decreases as $\ln(2\bar{A})^{-2}$. The value of $\langle S_{PI}\rangle/\left(n\langle S_{Hyd}\rangle\right)$ for fibers can be obtained from the numerical results of Mackaplow and Shaqfeh (1996) [23], where $\Delta\mu$ is given by

$$\frac{\Delta\mu}{\mu_f} = \frac{4\pi}{3}\frac{n}{\ln(2\bar{A})}\left(\frac{\ln(2\bar{A})+0.64}{\ln(2\bar{A})-1.5} + \frac{1.659}{\ln(2\bar{A})^2} + \frac{C_M}{\ln(2\bar{A})^2}n\right) \times \langle p_1^2 p_3^2\rangle, \tag{3.6}$$

where C_M is dependent on the orientation distribution and equals 0.444 for an isotropic orientation distribution and equals 0.412 for a nearly aligned fiber suspension [23]. Figure 6(f) shows the variation in $\langle S_{PI}\rangle/\left(n\langle S_{Hyd}\rangle\right)$ with the aspect ratio of the particle for rings and fibers with $C_M = 0.444$, suggesting that PIs lead to a greater increase in the suspension viscosity for rings than fibers at the same number density.

The value of $\Delta\mu/\mu_f$ for $\bar{A} = 10$ rings is of similar magnitude to the value obtained for $\bar{A} = 7$ disk suspension in Meng and Higdon's simulations as shown in Fig. 6(g) for $n \ll 1$. Meng and Higdon's simulations at lower concentrations are the only available data for disk suspensions that could serve as an approximation to the shear viscosity corrections with PI effects. The orientation statistics relative to the global frame

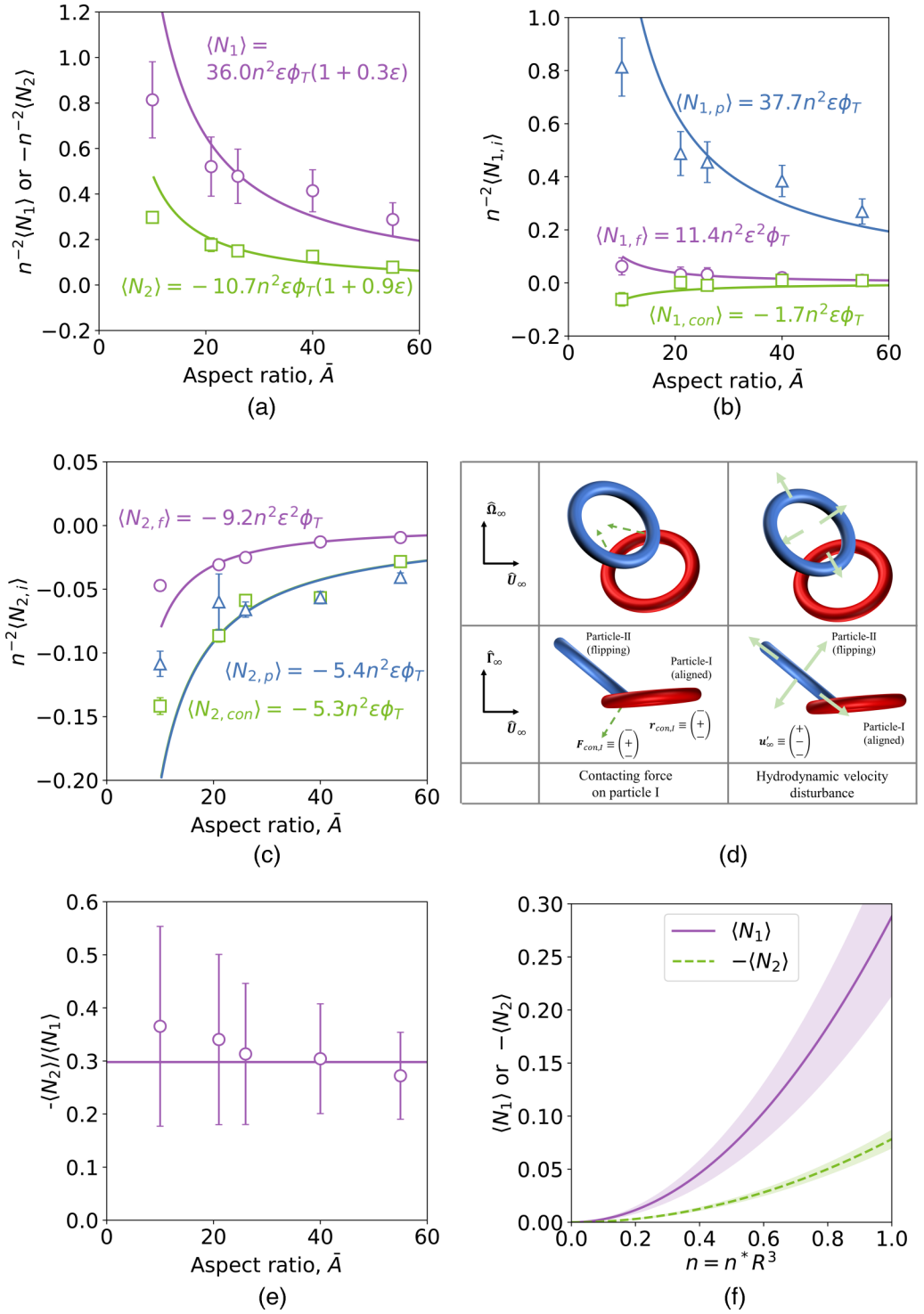

FIG. 7. (a) First, $\langle N_1\rangle$, and second, $\langle N_2\rangle$, normal stress difference as a function of the aspect ratio $\bar{A}$. (b) First and (c) second normal stress difference contributions from $\boldsymbol{S}_p$, $\boldsymbol{S}_f$, and $\boldsymbol{S}_{col}$ as functions of $\bar{A}$. (d) Schematic of interaction of two contacting rings to understand the relative contribution of normal stress differences from contact forces and $\boldsymbol{f}_{HI}$. (e) The ratio of the first and second normal stress difference $-\langle N_2\rangle/\langle N_1\rangle$ as a function of the aspect ratio that demonstrates that this ratio is $O(1)$ at moderately large aspect ratios ($10 \leq \bar{A} \leq 55$ in this study). The error bars for $\langle N_2\rangle/\langle N_1\rangle$ are equal to the sum of the standard errors of $\langle N_1\rangle$ and $\langle N_2\rangle$. (f) $\langle N_1\rangle$ and $\langle -N_2\rangle$ as a function of n for $\bar{A} = 55$ rings. All error bars and the shaded regions in (f) correspond to 95% confidence interval defined in Eq. (2.17).

was not available for the disk study to draw any further conclusions beyond this qualitative comparison.

E. Normal stresses from contacting trajectories

PIs of rings lead to non-zero normal stresses at $O(n^2)$, whereas isolated axisymmetric particles generate no normal stresses because of their symmetric orientation trajectories about the gradient-vorticity ($\hat{\boldsymbol{\Gamma}}_\infty - \hat{\boldsymbol{\Omega}}_\infty$) plane. Suspensions where particles have purely HIs also cannot have normal stresses because the microstructure again retains symmetry about the $\hat{\boldsymbol{\Gamma}}_\infty - \hat{\boldsymbol{\Omega}}_\infty$ plane and remains invariant upon reversal of the shear flow due to Stokes flow reversibility. A

collision breaks this reversibility because the contact force is non-zero when the particles approach each other and is zero when they move apart. This is a stark distinction from fiber suspensions for which collisions are rare at dilute concentrations and most interactions are purely hydrodynamic in nature. The first and second normal stress differences are given by $\langle N_1\rangle = n^2\,(\langle \boldsymbol{S}_{PI}\rangle/n)\,:(\hat{\boldsymbol{U}}_\infty\hat{\boldsymbol{U}}_\infty - \hat{\boldsymbol{\Gamma}}_\infty\hat{\boldsymbol{\Gamma}}_\infty)$ and $\langle N_2\rangle = n^2\,(\langle \boldsymbol{S}_{PI}\rangle/n)\,:(\hat{\boldsymbol{\Gamma}}_\infty\hat{\boldsymbol{\Gamma}}_\infty - \hat{\boldsymbol{\Omega}}_\infty\hat{\boldsymbol{\Omega}}_\infty)$, respectively, and their variation with the aspect ratio is shown in Fig. 7(a). $\langle N_1\rangle$ has a positive sign while $\langle N_2\rangle$ has a negative sign, and both scale with $\epsilon\phi_T$. The individual contributions to the normal stress differences from $\boldsymbol{S}_p$, $\boldsymbol{S}_f$, and $\boldsymbol{S}_{con}$ are given by $\langle N_{1,i}\rangle$ and $\langle N_{2,i}\rangle$ and shown in Figs. 7(b) and 7(c), where $i = \{p, f, con\}$. Particle contact leads to an $O(1)$ change in particle orientation relative to the Jeffery trajectory that results in $O(\epsilon\phi_T)$ contributions to $\langle N_{1,p}\rangle$ and $\langle N_{2,p}\rangle$. Similarly, the normal stresses from $\boldsymbol{f}_{HI}$ should be $O(\epsilon^2\phi_T)$ and the ones from contact forces should be $O(\epsilon\phi_T)$. The overall magnitude of the first normal stress difference is greater than the second normal stress difference. The asymptotic fit to the overall normal stresses based on the arguments above is given by

$$\langle N_1\rangle = 35.97n^2\epsilon\phi_T\,(1 + 0.32\epsilon), \tag{3.7}$$

$$\langle N_2\rangle = -10.68n^2\epsilon\phi_T\,(1 + 0.86\epsilon). \tag{3.8}$$

The signs and magnitudes of the normal stress differences can be understood from the microstructure of the particle suspension during a typical collision event. Let the stresslet $S_{i,kk}$ denote the normal stresses where $i = \{p, f, con\}$ and $k = \{1, 2, 3\} = \{\hat{\boldsymbol{U}}_\infty, \hat{\boldsymbol{\Omega}}_\infty, \hat{\boldsymbol{\Gamma}}_\infty\}$ on ring-I which is aligned near the flow-vorticity plane such that $|\boldsymbol{p}_I \cdot (\boldsymbol{I} - \hat{\boldsymbol{\Gamma}}_\infty\hat{\boldsymbol{\Gamma}}_\infty)| \ll 1$. A contact with a ring flipping in a $C \to \infty$ orbit would generate a contact force on ring-I with negative components in the flow and gradient directions if $\boldsymbol{r}_{con,I} \cdot \hat{\boldsymbol{U}}_\infty < 0$, $\boldsymbol{r}_{con,I}$ being the contact point relative to the center of mass of particle I. Thus, $S_{con,11}$ is negative and $S_{con,33}$ is positive leading to the unusual negative contribution to the first normal stress difference from contact stresses. The respective signs of the contact stresses for particle II are the same, and the argument also holds when $\boldsymbol{r}_{con,I} \cdot \hat{\boldsymbol{U}}_\infty > 0$. The simulations do predict the unusual negative value of $\langle N_{1,con}\rangle$ for $\bar{A} = 10$ rings, but the mean becomes comparable to the standard error for larger aspect ratio particles (the scaling coefficient for $\langle N_{1,con}\rangle$ was obtained using only $\bar{A} = 10$ ring simulation result). The values of normal stress differences from the transient orientation change relative to the Jeffery trajectory are given by

$$\frac{\langle N_{p,1}\rangle}{n^2} = -\frac{\xi_3}{4}\langle \sin^4(\theta)\sin(4\phi)\rangle = O(\xi_3\phi_T) > 0, \tag{3.9}$$

$$\begin{aligned}\frac{\langle N_{p,2}\rangle}{n^2} &= \frac{\xi_2}{2}\langle \sin^2(\theta)\sin(2\phi)\rangle \\ &\quad + \frac{\xi_3}{2}\langle \sin^2(\theta)\sin(2\phi)\,(\sin^2(\theta)\cos^2(\phi) - \cos^2(\theta))\rangle \\ &= -O(\phi_T(-|\xi_2| + \xi_3)) < 0,\end{aligned} \tag{3.10}$$

where we use the fact that $\langle -\phi\rangle = O(\phi_T)$ discussed in Sec. III C, $|\theta - \pi/2| \ll 1$ and $\xi_3 > |\xi_2|$. Both the sign and relative magnitudes of the normal stress differences from Eq. (3.8) are consistent with the values obtained from the numerical simulations.

Understanding the normal stresses induced by hydrodynamic interactions is a little more involved. A flipping ring with $\boldsymbol{p}_{II}$. $\hat{\boldsymbol{U}}_\infty > 0$ generates a velocity disturbance in a direction with $-\hat{\boldsymbol{\Gamma}}_\infty$, $+\hat{\boldsymbol{U}}_\infty$, and $-\hat{\boldsymbol{\Omega}}_\infty$ components near the point of contact as shown in Fig. 7(d). The corresponding induced hydrodynamic force per unit length on particle I near the point of contact should point in the opposite direction. Assuming that the signs of the normal stresses are consistent with the signs of local contributions to the stresslet, $S_{f,11}$ will be positive, $S_{f,22}$ positive, and $S_{f,33}$ negative, and there is no reason for any component to be much larger than the rest. Thus, the first normal stress difference should be positive and second normal stress difference should be negative, which is consistent with simulation results. The simulations also suggest that $\langle N_{p,1}\rangle > \langle N_{f,1}\rangle > |\langle N_{con,1}\rangle|$, while the relative order of magnitude is the same for different contributions for the second normal stress difference as shown in Figs. 7(b) and 7(c).

In this work, $\langle N_2\rangle$ was found to be of the same order of magnitude as $\langle N_1\rangle$, which is contrary to the common assumption used in fiber suspensions that $|\langle N_2\rangle| \ll \langle N_1\rangle$ [14,7]. Interestingly, recent experimental findings and simulations of semiconcentrated fiber suspensions have also found comparable magnitudes of $\langle N_1\rangle$ and $|\langle N_2\rangle|$ [29,45]. However, the mechanism leading to this result is different for the two cases. In fibers, Snook and coworkers argue that the major contribution to first and second normal stress differences arises from the contact forces acting on the particles. This differs from our work on dilute rings as the contact contribution is comparable to, or in the case of $\langle N_{con,1}\rangle$ even smaller than, hydrodynamic contributions $(\langle N_{p,1}\rangle$ and $\langle N_{f,1}\rangle)$. The contact contribution is large in semiconcentrated fiber suspensions potentially due to multiparticle contacts and the aligned microstructure. Most interactions in concentrated fibers would be associated with highly aligned fibers, and thus, the hydrodynamic contribution would be smaller than the contact part.

The current simulation results suggest a nearly constant value of $\langle N_2\rangle/\langle N_1\rangle$ as shown in Fig. 7(e) where the solid line is a constant value of ~0.3 obtained from the scaling arguments in Eqs. (3.7) and (3.8) in the limit as $\epsilon \to 0$. The magnitude of the normal stresses as a function of number density is shown in Fig. 5(f) for $\bar{A} = 55$ rings. The normal stresses in Fig. 5(f) at $n = O(1)$ have magnitudes that are comparable to the experimentally measured values in semiconcentrated suspensions for equivalent fiber suspensions ($\langle N_1\rangle \approx 0.027$ at $n = 0.37\bar{A}$ for $\bar{A} = 57$ fibers from Carter's experiment) [46,29,28]. This suggests that the normal stresses in dilute ring suspensions arising only from pairwise contact should have sufficiently large magnitude to be observed experimentally.

F. Shear rate dependence of the rheology for isolated Brownian rings

Brownian dynamics simulations on isolated rings were performed to obtain the shear rate dependence of suspension

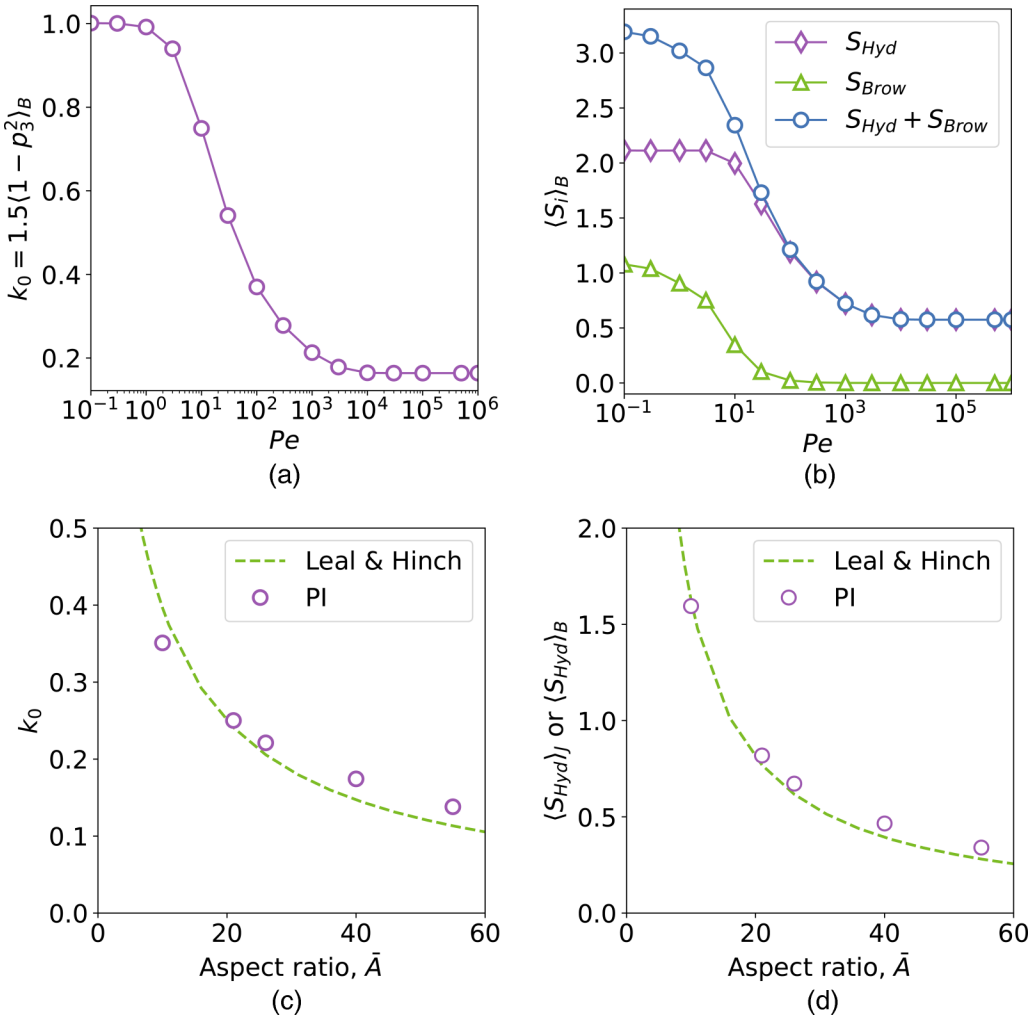

FIG. 8. (a) The flow-alignment parameter as a function of Peclet number, Pe. (b) The two contributions of the stresslet $\langle \boldsymbol{S}_{Brow} \rangle$ and $\langle \boldsymbol{S}_{Hyd} \rangle$ as a function of Pe. The aspect ratio of the ring is $A = 26$ corresponding to $\lambda = -1 + 8.62 \times 10^{-3}$. (c) k_0 and (d) $\langle S_{Hyd} \rangle_B$ and $\langle S_{Hyd} \rangle_J$ obtained from the Leal and Hinch distribution valid at $Pe \gg \phi_T^{-3}$ and the distribution from pairwise interactions.

rheology at $O(n)$ using the procedure discussed in Appendix A.2. Brownian motion drives the suspension toward an isotropic orientation distribution and competes with the SSF that tries to distort the distribution through Jeffery rotation. The alignment of the ring under the influence of Brownian motion can also be quantified using the flow-alignment parameter $k_0 = 1.5\big(1 - \langle \boldsymbol{pp}{:}\hat{\boldsymbol{\Gamma}}_\infty \hat{\boldsymbol{\Gamma}}_\infty \rangle_B\big)$, which provides the tilt of the ring relative to the flow-vorticity plane. The $\langle\rangle_B$ represent an ensemble average across the orientation distribution resulting from shear and Brownian motion. Figure 8(a) shows the variation in k_0 with Pe. Here, $k_0 = 1$ for $Pe \ll 1$ associated with the isotropic distribution of $\boldsymbol{p}$. The value of $k_0 \propto Pe^{-1/3}$ for $1 \ll Pe \ll \phi_T^{-3}$ where the 1/3 power law is obtained from the boundary layer analysis of the Fokker–Planck equation for the orientation probability distribution discussed in [47]. The value of k_0 plateaus in the high-Pe limit, $Pe \gg \phi_T^{-3}$, to a value of $O(\phi_T)$ that can be obtained directly from the analysis of [30].

Brownian motion influences the hydrodynamic stresslet tensor $\langle \boldsymbol{S}_{Hyd} \rangle_B$ through changes in $\boldsymbol{p}$, but also has a more direct contribution termed the Brownian stresslet tensor $\langle \boldsymbol{S}_{Brow} \rangle_B = 3Pe^{-1} M_r^{-1} \lambda \big(\langle \boldsymbol{pp} \rangle_B - \boldsymbol{I}/3 \big)$ that arises by virtue of an angular velocity associated with the diffusion process across the gradients in the orientation probability distribution [47]. Here, $M_r = (2 - 3\epsilon)/(8\pi^2 \epsilon)$ is the non-dimensional rotary mobility of the axisymmetric ring [31]. The relative increase in the suspension viscosity $\Delta\mu/\mu_f$ is equal to $n\big(\langle S_{Brow} \rangle_B + \langle S_{Hyd} \rangle_B\big)$, where $\langle S_{Hyd} \rangle_B = \langle \boldsymbol{S}_{Hyd} \rangle_B {:} \hat{\boldsymbol{U}}_\infty \hat{\boldsymbol{\Gamma}}_\infty$ and $\langle S_{Brow} \rangle_B = \langle \boldsymbol{S}_{Brow} \rangle_B {:} \hat{\boldsymbol{U}}_\infty \hat{\boldsymbol{\Gamma}}_\infty$. The values of $\langle S_{Brow} \rangle_B$ and $\langle S_{Hyd} \rangle_B$ as functions of Pe are shown in Fig. 8(b), which exhibit the well-known shear thinning behavior expected for dilute particle suspensions [18].

The orientation distribution in the shear dominated flows $Pe \gg \phi_T^{-3}$ can be fully described by an orbit distribution and Jeffery rotation [30]. In this flow regime, the order parameter and the particle shear stress can be obtained as a function of $\bar{A}$ by directly using the orbit distribution from Leal and Hinch [30] (i.e., the LH distribution). Figure 8(c) shows the value of k_0 from the LH distribution that is slightly lower than the k_0 obtained from the PI distribution discussed in Sec. III C for $\bar{A} > 26$. This is because the probability distribution of the modified orbit constant $p(C_b = C/(C+1))$ from PIs is less peaked near $C \to \infty$ compared to the LH distribution at high aspect ratios as shown in Fig. 4(b). For

$\bar{A} = 10$, the distribution from PI had a higher peak near the $C \to \infty$ orbit and, thus, a lower k_0 compared to the value obtained from the LH distribution. A similar trend also holds for the particle shear stress shown in Fig. 6(d). The particle shear stress generated from the LH distribution is similar to PI distribution results of Sec. III D near $\bar{A} = 21$, because of the similarities of the two distributions. Numerically, $\langle S_{Hyd} \rangle_B$ for an $\bar{A} = 55$ particle computed from the LH distribution was only 16% lower than $\langle S_{Hyd} \rangle_J$ computed from the orbit distribution from PIs. This similarity results from the fact that the PI orbit distribution driven by large changes in the orientation during particle collisions is surprisingly similar to the LH orbit distribution caused by small Brownian rotations.

The non-Brownian particle rheology described in Secs. III B–III E should also be accurate for Brownian rings when the relaxation time of the orientation distribution due to Brownian motion, $Pe\phi_T^2$, is much larger than the $O(n^{-1})$ relaxation time set by pairwise interactions. Thus, for $Pe^{-1}\phi_T^{-2} \ll n \ll 1$, the viscosity correction and normal stresses described by the pairwise calculation for non-Brownian rings should also be representative for a suspension of weakly Brownian rings ($Pe \gg \phi_T^{-3}$). Due to the similarity of the orbit distribution set by weak Brownian motion $Pe \gg \phi_T^{-3}$ and PIs, the non-Brownian rheology calculations should be applicable at all dilute concentrations, i.e., $n \ll 1$, if $Pe \gg \phi_T^{-3}$.

IV. CONCLUSIONS

In this work, the orientational structure and rheology of a sheared suspension of high-aspect ratio ($\bar{A} = 10-55$) non-Brownian rings were calculated at dilute concentrations using numerical simulations. Particle contact has a small influence on the rheology of a suspension of high-aspect ratio fibers at dilute concentrations ($n \ll 1$) but plays a critical role in describing the rheology of a suspension of planar particles such as rings. The present work is the first attempt at quantifying the effect of particle contact at $n \ll 1$ using dynamic simulations accounting for pairwise long-range hydrodynamic interactions (HIs) through slender-body-theory formulation and particle contact using a short-range repulsive force. The $O(1)$ change in the particle orientation from contact is much larger than the $O([\ln(8\bar{A})]^{-1})$ change from purely hydrodynamic interactions. Surprisingly, the orientational structure of ring suspensions was found to be qualitatively similar to the structure in an equivalent suspension of hydrodynamically interacting fibers (with an angular rotation of $\pi/2$ in ϕ). We evaluated the steady state Jeffery orbit distribution for rings that can be used to calculate an $O(1)$ anisotropic structure of the materials processed using sheared ring-suspensions. Pairwise interactions increase the dispersion of the orientation from Jeffery rotation and also lead to an average displacement of the orientation away from the flipping orbits ($C \to \infty$) during the interaction.

The leading order contribution to the relative suspension viscosity ($\Delta\mu/\mu_f$) obtained from the steady state orbit distribution was found to be approximately given by $n\langle S_{Hyd} \rangle_J = 54.88\epsilon\phi_T n$ in the aspect ratio range studied here. The $O(n^2)$ correction to $\Delta\mu/\mu_f$ had three components, one associated with the transient deviation of the particle orientation from a Jeffery trajectory, $n\langle S_p \rangle = 38.99n^2\epsilon\phi_T(1 + 3.16\epsilon)$; a direct contribution from contact forces $n\langle S_{con} \rangle = 10.17n^2\phi_T\epsilon$; and a contribution from the velocity disturbance produced by neighboring rings $n\langle S_f \rangle = 51.68n^2\phi_T\epsilon^2$. Numerically, the strength of pairwise interactions of rings was much greater than the pairwise interactions of equivalent fibers, seen from the ratio of $O(n^2)$ and $O(n)$ coefficients of $\Delta\mu/\mu_f$ for the two systems. The value of $\Delta\mu/\mu_f$ for $\bar{A} = 10$ rings was found to be of the same magnitude as the value obtained from numerical simulations for $\bar{A} = 7$ disks, indicating that disks and ring suspensions have similar particle shear stresses in the dilute limit.

The dilute suspension of rings has non-zero normal stress differences because of symmetry breaking from particle contacts. The first normal stress difference was positive and the second normal stress difference was negative, and both scaled as $O(n^2\epsilon\phi_T)$. $\langle N_1 \rangle = 37.4n^2\epsilon\phi_T\,(1 + 0.3\epsilon)$ and $\langle N \rangle_2 = -10.6n^2\epsilon\phi_T\,(1 + 0.9\epsilon)$ were the best fits to simulation data. $\langle N_1 \rangle$ and $\langle N_2 \rangle$ were found to be of comparable magnitudes for ring suspensions and similar observations have recently been reported for fiber suspensions at $n = O(\bar{A})$, although the physical mechanism is different for the two cases as explained in Sec. III E.

The contact frequency of rings per unit volume was also found to be equal to $4.37n^2\phi_T$ in the aspect ratio range, $10 \le \bar{A} \le 55$. The shape of the collision cross section in the vorticity-gradient plane was close to the one expected between a tumbling and an aligned ring. Furthermore, the diffusive motion of the center of mass of a ring through the suspension was quantified through a hydrodynamic diffusivity in the gradient (D_{33}) and vorticity (D_{22}) directions. The approximate relations $D_{22} = 3.17 \times 10^{-2}\phi_T + 5.60\epsilon^2\phi_T$ and $D_{33} = 4.16 \times 10^{-2}\,\phi_T + 1.39\,\epsilon^2\phi_T$ fit the simulation data well for $21 \le \bar{A} \le 55$. At the same concentration, these hydrodynamic diffusivities were found to be two orders of magnitude larger than corresponding values for equivalent fibers suggesting greater dispersion of rings in a channel flow compared to fibers.

The dependence of rheology of dilute ring suspensions on the shear rate was also established through Brownian dynamics simulation of isolated rings. The flow-aligning parameter, k, monotonically decreased from unity for $Pe \ll 1$ to a plateau value of $O(\phi_T)$ at $Pe \gg \phi_T^{-3}$. Suspensions of Brownian rings at low concentration exhibit shear thinning behavior with the $O(n\epsilon)$ low-Pe plateau of $\Delta\mu/\mu_f$ being larger than the $O(n\phi_T\epsilon)$ high-Pe plateau by a factor of $O(\phi_T)$. The orbit distribution set by weak Brownian motion $Pe \gg \phi_T^{-3}$ was found to be similar to the distribution set by pairwise interactions. This implies that the viscosity corrections and normal stresses in this shear-dominated flow-regime should be well represented by the pairwise interaction results for non-Brownian particles in Sec. III at all dilute concentrations $n \ll 1$ and $Pe \gg \phi_T^{-3}$.

The results presented here should deviate from reality at concentrations $n = O(1)$. Our calculations suggest that pairwise interactions decrease the flow-alignment at low n. At

high enough number densities, excluded volume interactions become important and this should enhance the flow-alignment. Therefore, the dispersion in $\boldsymbol{p}$ should reach a peak value at an intermediate number density. This behavior would be qualitatively similar to fiber suspensions wherein $\langle\cos^2(\phi)\rangle - \langle\cos^2(\phi)\rangle_J$ has been experimentally observed to increase with n in the dilute regime, reach a peak value at $n\bar{A}^{-1} = 0.06 - 0.1$, and decrease at concentrations greater than $n\bar{A}^{-1} \geq 0.1$ due to excluded volume interactions [28]. Multiparticle contacts at $n = O(1)$ in ring suspensions should also have qualitative similarity to fiber-suspensions wherein the normal stresses were generated mainly by contact forces and the particle shear stresses are mainly driven by hydrodynamic velocity disturbances [29].

The rheology and structure of ring suspensions at higher concentrations could be obtained experimentally at different shear rates. The rings themselves can be fabricated using various techniques such as vortex ring freezing [48] and photolithography [49,50]. The current simulation strategy can also be used to study rings with noncircular cross sections some of which can self-align without application of external forces or torques [37]. Suspensions of such aligning particles should have different rheological properties than those for the tumbling rings studied in this work. The $O(n^2)$ corrections to rheology of Brownian particles could also be obtained for shear-dominated flows, $Pe \gg 1$, by incorporating rotational and translational diffusion into the simulation strategy in Sec. II. The initial orientation of the particles could be computed using a strategy similar to the one described in Sec. II D.

The current work provides new insight into dilute particle rheology that is usually assumed to be solely determined by purely hydrodynamic interactions. In general, particle contact should also be important in determining suspension rheology at dilute concentrations ($Pe^{-1}\phi_T^{-2} \ll n \ll 1$) for most high-aspect ratio particles other than the special case of the suspension of *straight* fibers. The current simulation strategy could be extended to any rigid high-aspect ratio filamentous shape by including two additional orientational degrees of freedom, thus greatly expanding on the range of possible shapes whose rheology can be accurately captured at dilute concentrations.

ACKNOWLEDGMENTS

This work was supported by NSF under Grant No. 2206851.

AUTHOR DECLARATIONS

Conflicts of Interest

The authors have no conflicts to disclose.

DATA AVAILABILITY

The data that support the findings of this study are available from the corresponding author upon reasonable request.

APPENDIX: SBT ACCURACY AND BD SIMULATION STRATEGY

1. Stresslet tensor and force-per-unit length for an isolated torus

The geometric parameters ξ_i required to compute the hydrodynamic stresslet from Eq. (2.20) are given by

$$\xi_1 = 8\pi^2\left(\left(1+\frac{1}{2A^2}\right)\left(\frac{(-f_{n1}+f_{b4})}{\gamma_1}\right)+\frac{1}{2A^2}\right),$$
$$\xi_2 = -\xi_1 + \frac{10\pi^2}{A^2}\left(1-\frac{3}{5\epsilon A^2}(1-1.5\epsilon)\right),$$
$$\xi_3 = -8\pi^2\left(1+\frac{1}{2A^2}\right)\frac{f_{n1}}{\gamma_1} - \frac{6\pi^2}{A^2}\left(1-\frac{2}{\epsilon A^2}(1-1.5\epsilon)\right), \tag{A1.1}$$

where $f_{n1}/\gamma_1 = -\frac{7\epsilon}{16}\frac{\left(1-\frac{16}{3}\epsilon+\frac{1211}{180}\epsilon^2\right)}{\left(1-\frac{151}{30}\epsilon+\frac{514}{90}\epsilon^2\right)\left(1-\frac{5}{2}\epsilon\right)}$ and $f_{b4}/\gamma_1 = -\frac{\epsilon}{16}\frac{\left(1-\frac{88}{30}\epsilon-\frac{253}{180}\epsilon^2\right)}{\left(1-\frac{151}{30}\epsilon+\frac{514}{90}\epsilon^2\right)\left(1-\frac{5}{2}\epsilon\right)}$ [34]. Equation (A 1.1) is derived by using the inner velocity field ($\boldsymbol{u}_{inner}$) in SBT formulation to compute the stress $\boldsymbol{\sigma}$ and integrating over the particle surface A_p to find the stresslet given mathematically by

$$\langle \boldsymbol{S}_{Hyd}\rangle = \oiint_{A_p} dA\left(\frac{\boldsymbol{r}(\boldsymbol{\sigma}\cdot\breve{\boldsymbol{n}})+(\boldsymbol{\sigma}\cdot\breve{\boldsymbol{n}})\boldsymbol{r}}{2} - \frac{\boldsymbol{\sigma}\cdot\breve{\boldsymbol{n}}\boldsymbol{r}}{3}\boldsymbol{I}\right). \tag{A1.2}$$

Here, $\breve{\boldsymbol{n}}$ is the unit normal to the particle surface and $\boldsymbol{r}$ is the position vector. The integration yields a stresslet of the form given in Eq. (2.20) with coefficients in (A1.1) with accuracy including terms up to $O(A^{-2})$. These coefficients compare well with values obtained from boundary element method simulations for $A \geq 10$ as shown in Fig. 9.

The force per unit length is given by $f_n = f_{n1}\cos(s) + f_{n3}\cos(3s)$, $f_b = f_{b4}\sin(s) + f_{n3}\sin(3s)$, and $f_p = 0$, $0 \leq s < 2\pi$. The coefficients f_{n1}, f_{n3}, and f_{b4} as a function of the aspect ratio are shown in Fig. 9 for a force and torque free ring rotating in the $C \to \infty$ orbit as obtained from the SBT of [34] (solid-lines) and BEM [51] (symbols). The SBT values match closely with BEM simulations (symbols) for $\bar{A} \geq 10$ shown as a dashed line in Fig. 9.

2. Brownian Dynamics (BD) simulation strategy for Isolated Brownian rings

Rotary Brownian dynamics simulations of axisymmetric rings with rotary diffusivity $D_r = k_B T_B(2-3\epsilon)/(8\pi^2\mu_f\epsilon R^3)$ [31] were carried out to obtain the shear rate dependence of stresses in suspension [52]. Here, T_B is the temperature of the fluid and k_B is the Boltzmann constant. As shown in Sec. II D, the orbit distribution of weakly Brownian rings ($Pe = \gamma/D_r \gg \phi_T^{-3}$) is similar to orbit distribution obtained from pairwise simulations. The calculation provides a measure of a critical rotary Peclet number $Pe = O(\phi_T^{-3})$ for

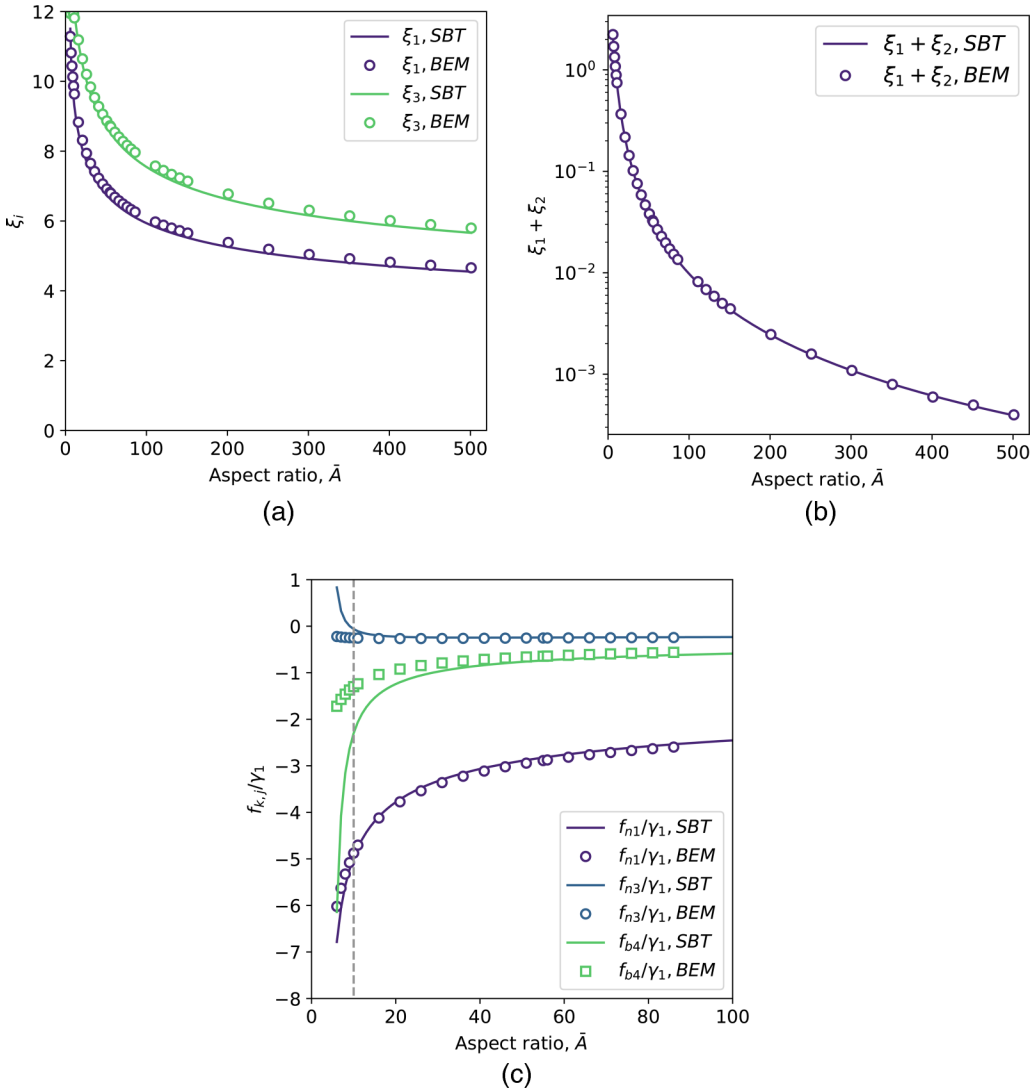

FIG. 9. (a) Geometric coefficients (a) ξ_1 and ξ_3 (b) $(\xi_1+\xi_2)$, which is $O(A^{-2})$, obtained from slender-body-theory (solid-lines) and boundary element method simulations (symbols). (c) The force per unit length for a force or torque-free particle in the $C \to \infty$ orbit is given by $f_n = f_{n1}\cos(s) + f_{n3}\cos(3s)$, $f_b = f_{b4}\sin(s) + f_{n3}\sin(3s)$, and $f_p = 0$, $0 \le s < 2\pi$. The dashed line corresponds to $\bar{A} = 10$.

which this holds true. The orientation parameter and particle stresses are also provided as a function of Pe.

The rotational displacement at each Brownian time step Δt_B (non-dimensional) is given by

$$\boldsymbol{p}(t+\Delta t_B) - \boldsymbol{p}(t) = \int_t^{t+\Delta t_B} dt' \left[\dot{\boldsymbol{p}}_{\boldsymbol{J}}(t') + \frac{\Delta \boldsymbol{p}_{\boldsymbol{B}}(t)}{\Delta t_B} \right], \qquad \text{(A2.1)}$$

where $\dot{\boldsymbol{p}}_{\boldsymbol{J}} = \boldsymbol{p}\cdot\boldsymbol{R}_\infty + \lambda(\boldsymbol{E}_\infty\cdot\boldsymbol{p} - \boldsymbol{E}_\infty{:}\boldsymbol{ppp})$ is the rotation rate induced by the SSF. The Brownian displacement $\Delta\boldsymbol{p}_{\boldsymbol{B}}$ is such that $\langle \Delta\boldsymbol{p}_{\boldsymbol{B}}\rangle = 0$, $\langle \Delta\boldsymbol{p}_{\boldsymbol{B}}\Delta\boldsymbol{p}_{\boldsymbol{B}}\rangle = (2D_r\Delta t_B)^{0.5}(\boldsymbol{I}-\boldsymbol{pp})$. The quantity $P(\boldsymbol{p})\boldsymbol{dp}$ gives the fraction of rings in the differential region $\boldsymbol{dp}$ around $\boldsymbol{p}$ and is used to obtain the ensemble average of any quantity of interest $\boldsymbol{X}$, which is given by

$$\langle \boldsymbol{X}\rangle_B = \int \boldsymbol{dp}\; P(\boldsymbol{p})\boldsymbol{X}. \qquad \text{(A2.2)}$$

A Runge–Kutta method with an adaptive time stepping method was used to solve the integral equation (4.1) during each Brownian step Δt_B. The mean squared value of the angular step is given by $\sqrt{2\Delta t_B/Pe}$. For $Pe < 1$, a variable Brownian time step $\Delta t_B = 10^{-2}Pe$ guarantees that the mean-squared value of the Brownian angular step, $\sqrt{2\Delta t_B/Pe}$, is smaller than unity. For $Pe > 1$, the time step is chosen to be $\Delta t_B = 10^{-2}$, which satisfies the condition $\sqrt{2\Delta t_B/Pe} \ll \phi_T$ for $Pe \gg 1$ and $\sqrt{2\Delta t_B/Pe} \ll 1$ for $Pe \gtrsim \mathrm{O}(1)$. The steady-state orientation distribution is attained in an $O(Pe)$ time for $Pe \ll 1$ and an $O(Pe\ \phi_T^2)$ time for $Pe \gg 1$ [53]. The simulation was terminated after a time 10^5 for $1 \le Pe \le 10^5$ and after a time $10^5 Pe$ for $Pe < 1$.

REFERENCES

[1] Mansouri, J., R. P. Burford, Y. B. Cheng, and L. Hanu, "Formation of strong ceramified ash from silicone-based compositions," J. Mater. Sci. **40**(21), 5741–5749 (2005).

[2] De, S., T. M. Higgins, P. E. Lyons, E. M. Doherty, P. N. Nirmalraj, W. J. Blau, J. J. Boland, and J. N. Coleman, "Silver nanowire networks as flexible, transparent, conducting films: Extremely high DC to optical conductivity ratios," ACS Nano **3**(7), 1767–1774 (2009).

[3] Lundell, F., L. D. Söderberg, and P. H. Alfredsson, "Fluid mechanics of papermaking," Annu. Rev. Fluid Mech. **43**, 195–217 (2011).

[4] Einstein, A., "Eine neue bestimmung der moleküldimensionen," Ann. Phys. **324**(2), 289–306 (1906).

[5] Denn, M. M., and J. F. Morris, "Rheology of non-Brownian suspensions," Annu. Rev. Chem. Biomol. Eng. **5**(1), 203–228 (2014).

[6] Stickel, J. J., and R. L. Powell, "Fluid mechanics and rheology of dense suspensions," Annu. Rev. Fluid Mech. **37**(1), 129–149 (2005).

[7] Petrie, C. J. S., "The rheology of fibre suspensions," J. Non-Newtonian Fluid Mech. **87**(2-3), 369–402 (1999).

[8] Butler, J. E., and B. Snook, "Microstructural dynamics and rheology of suspensions of rigid fibers," Annu.Rev. Fluid Mech. **50**(1), 299–318 (2018).

[9] Yamamoto, S., and T. Matsuoka, "Dynamic simulation of a plate-like particle dispersed system," J. Chem. Phys. **107**, 3300–3308 (1997).

[10] Meng, Q., and J. J. L. Higdon, "Large scale dynamic simulation of plate-like particle suspensions: Part I: Non-Brownian simulation," J. Rheol. **52**(1), 1–36 (2008).

[11] Anczurowski, E., and S. G. Mason, "Particle motions in sheared suspension: XXIV. Rotations of rigid spheroids and cylinders," Trans. Soc. Rheol. **12**, 209–215 (1968).

[12] Jogun, S., and C. F. Zukoski, "Rheology of dense suspensions of plate-like particles," J. Rheol. **40**, 1211–1232 (1996).

[13] Jogun, S. M., and C. F. Zukoski, "Rheology and microstructure of dense suspensions of plate-shaped colloidal particles," J. Rheol. **43**, 847–871 (1999).

[14] Zirnsak, M. A., D. U. Hur, and D. V. Boger, "Normal stresses in fibre suspensions," J. Non-Newtonian Fluid Mech. **54**, 153–193 (1994).

[15] White, K. L., S. Hawkins, M. Miyamoto, A. Takahara, and H.-J. Sue, "Effects of aspect ratio and concentration on rheology of epoxy suspensions containing model plate-like nanoparticles," Phys. Fluids **27**, 123306 (2015).

[16] Brown, A. B. D., S. M. Clarke, P. Convert, and A. R. Rennie, "Orientational order in concentrated dispersions of plate-like kaolinite particles under shear," J. Rheol. **44**(2), 221–233 (2000).

[17] Singh, V., D. L. Koch, and A. D. Stroock, "Ideal rate of collision of cylinders in simple shear flow," Langmuir **27**(19), 11813–11823 (2011).

[18] Brenner, H., "Rheology of a dilute suspension of axisymmetric Brownian particles," Int. J. Multiphase Flow **1**(2), 195–341 (1974).

[19] Avendañoa, C., G. Jackson, E. A. Müller, and F. A. Escobedo, "Assembly of porous smectic structures formed from interlocking high-symmetry planar nanorings," Proc. Natl. Acad. Sci. U.S.A. **113**(35), 9699–9703 (2016).

[20] Qi, G., L. Fu, and E. P. Giannelis, "Sponges with covalently tethered amines for high-efficiency carbon capture," Nat. Commun. **5**, 5796 (2014).

[21] Lu, P., and Y. Xia, "Maneuvering the internal porosity and surface morphology of electrospun polystyrene yarns by controlling the solvent and relative," Langmuir **29**(23), 7070–7078 (2013).

[22] Haase, M., H. Jeon, N. Hough, J. K. Kim, K. J. Stebe, and D. Lee, "Multifunctional nanocomposite hollow fiber membranes by solvent transfer induced phase separation," Nat. Commun. **8**(1), 1234 (2017).

[23] Mackaplow, M., and E. S. G. Shaqfeh, "A numerical study of the rheological properties of suspensions of rigid, non-Brownian fibres," J. Fluid Mech. **329**, 155–186 (1996).

[24] Rahnama, M., D. L. Koch, and E. S. G. Shaqfeh, "The effect of hydrodynamic interactions on the orientation distribution in a fiber suspension subject to simple shear flow," Phys. Fluids **7**(3), 487–506 (1995).

[25] Bibbo, M. A., Rheology of semiconcentrated fibre suspensions, Ph.D. thesis, Massachusetts Institute of Technology, 1987.

[26] Claeys, I. L., and J. F. Brady, "The dynamics of prolate spheroids in stokes flow: Part 2. Statistically homogeneous dispersions," J. Fluid Mech. **251**, 443–477 (1993).

[27] Sundararajakumar, R. R., and D. L. Koch, "Structure and properties of sheared fiber suspensions with mechanical contacts," J. Non-Newtonian Fluid Mech. **73**(3), 205–239 (1997).

[28] Petrich, M. P., D. L. Koch, and C. Cohen, "An experimental determination of the stress–microstructure," J. Non-Newtonian Fluid Mech. **95**, 101–133 (2000).

[29] Snook, B., L. M. Davidson, J. E. Butler, O. Pouliquen, and É Guazzelli, "Normal stress differences in suspensions of rigid fibres," J. Fluid Mech. **758**, 486–507 (2014).

[30] Leal, L. G., and E. J. Hinch, "The effect of weak Brownian rotations on particles in shear flow," J. Fluid Mech. **46**(4), 685–703 (1971).

[31] Johnson, R. E., and T. Y. Wu, "Hydrodynamics of low-Reynolds-number flow, part 5.: Motion of a slender torus," J. Fluid Mech. **95**, 263–277 (1979).

[32] Jeffery, G. B., "The motion of ellipsoidal particles immersed in a viscous fluid," Proc. R. Soc. London A **102**(715), 161–179 (1922).

[33] Bretherton, F. P., "The motion of rigid particles in a shear flow at low Reynolds number," J. Fluid Mech. **14**, 284–304 (1962).

[34] Borker, N. S., and D. L. Koch, "Slender body theory for particles with non-circular cross-sections with applications to particle dynamics in shear flows," J. Fluid Mech. **877**, 1098–1133 (2019).

[35] Singh, V., D. L. Koch, G. Subramanian, and A. D. Stroock, "Rotational motion of a thin axisymmetric disk in a low Reynolds number linear flow," Phys. Fluids **26**(3), 033303 (2014).

[36] Cox, R. G., "The motion of long slender bodies in a viscous fluid.: Part 2. Shear flow," J. Fluid Mech. **45**(4), 625–657 (1971).

[37] Singh, V., D. L. Koch, and A. D. Stroock, "Rigid ring-shaped particles that align in simple shear flow," J. Fluid Mech. **722**, 121–158 (2013).

[38] Yamane, Y., Y. Kaneda, and M. Doi, "Numerical simulation of semi-dilute suspensions of rodlike particles in shear flow," J. Non-Newtonian Fluid Mech. **54**, 405–421 (1994).

[39] Harlen, O. G., R. R. Sundararajakumar, and D. L. Koch, "Numerical simulations of a sphere settling through a suspension of neutrally buoyant fibres," J. Fluid Mech. **388**, 355–388 (1999).

[40] Da Cunha, F. R., and E. J. Hinch, "Shear-induced dispersion in a dilute suspension of rough spheres," J. Fluid Mech. **309**, 211–223 (1996).

[41] Rahnama, M., D. L. Koch, Y. Iso, and C. Cohen, "Hydrodynamic, translational diffusion in fiber suspensions subject to simple shear flow," Phys. Fluids A **5**(4), 849–862 (1993).

[42] Kim, S., and S. Karilla, *Microhydrodynamics* (Dover, Mineola, New York, 1991).

[43] Batchelor, G. K., and J. T. Green, "The determination of the bulk stress in a suspension of spherical particles to order c^2," J. Fluid Mech. **56**(3), 401–427 (1972).

[44] Stover, C. A., D. L. Koch, and C. Cohen, "Observations of fibre orientation in simple shear flow of semi-dilute suspensions," J. Fluid Mech. **238**, 277–296 (1992).

[45] Bounoua, S., P. Kuzhir, and E. Lemaire, "Normal stress differences in non-Brownian fiber suspensions," J. Rheol. **60**(4), 661–671 (2016).

[46] Carter, L. F., and J. Goddard, "A rheological study of glass fibers in a Newtonian oil," NASA Report No. N67-30073, 1967.

[47] Hinch, E. J., and L. G. Leal, "The effect of Brownian motion on the rheological properties of a suspension of non-spherical particles," J. Fluid Mech. **52**(4), 683–712 (1972).

[48] An, D., A. Warning, K. G. Yancey, C.-T. Chang, V. R. Kern, A. K. Datta, P. H. Steen, D. Luo, and M. Ma, "Mass production of shaped particles through vortex ring freezing," Nat. Commun. **7**, 12401 (2016).

[49] Foulds, I. G., and M. Parameswaran, "A planar self-sacrificial multilayer SU-8-based MEMS process utilizing a UV-blocking layer for the creation of freely moving parts," J. Micromech. Microeng. **16**(10), 2109–2115 (2006).

[50] Branch, R. J., "Two-step photolithography for fabrication of high aspect ratio SU-8 rings," *2015-2016 Cornell NanoScale Facility (CNF) Research Accomplishments* (Cornell NanoScale Facility, Ithaca, NY, 2016), pp. 202–203, see https://cnf.cornell.edu/publications/research_accomplishments.

[51] Borker, N. S., A. D. Stroock, and D. L. Koch, "Controlling rotation and migration of rings in a simple shear flow through geometric modifications," J. Fluid Mech. **840**, 379–407 (2018).

[52] Gabdoulline, R. R., and R. C. Wade, "Brownian dynamics simulation of protein–protein diffusional encounter," Methods **14**(3), 329–341 (1998).

[53] Leahy, B., D. L. Koch, and I. Cohen, "The effect of shear flow on the rotational diffusion of a single axisymmetric particle," J. Fluid Mech. **772**, 42–79 (2015).

[54] See supplementary material at https://www.scitation.org/doi/suppl/10.1122/8.0000628 for videos of contacting and non-contacting trajectories of pairwise interacting rings.